Neuron

Article

Opioid-driven disruption of the septum reveals a role for neurotensin-expressing neurons in withdrawal

Highlights

- The LS regulates motivated behaviors and is implicated in substance use disorders
- Naloxone activates LS-*Nts* neurons in opioid-dependent mice
- Opioid withdrawal enhances LS-*Nts* activity through elevated glutamatergic signaling
- LS-*Nts* neurons alter pain expression and sociability during opioid withdrawal

Authors

Rhiana C. Simon, Weston T. Fleming, Brandy A. Briones, ..., Andrea D. Sanders, Sam A. Golden, Garret D. Stuber

Correspondence

gstuber@uw.edu

In brief

Opioid withdrawal produces a dysphoric state that can lead to relapse. Simon et al. reveal that lateral septal neurotensin-expressing neurons are selectively activated by naloxone and drive changes in pain coping and sociability in opioid-dependent mice, highlighting the potential role for the lateral septum in regulating behavior during opioid withdrawal.

Simon et al., 2025, Neuron *113*, 1–19
July 23, 2025
https://doi.org/10.1016/j.neuron.2025.04.024

CellPress

Please cite this article in press as: Simon et al., Opioid-driven disruption of the septum reveals a role for neurotensin-expressing neurons in withdrawal, Neuron (2025), https://doi.org/10.1016/j.neuron.2025.04.024

Neuron

CellPress

Article

Opioid-driven disruption of the septum reveals a role for neurotensin-expressing neurons in withdrawal

Rhiana C. Simon,[1,2] Weston T. Fleming,[1,2,3] Brandy A. Briones,[1,2] Marta Trzeciak,[1,2] Pranav Senthilkumar,[1] Kentaro K. Ishii,[1,2] Madelyn M. Hjort,[1,2] Madison M. Martin,[1,2] Koichi Hashikawa,[1,2] Andrea D. Sanders,[1] Sam A. Golden,[1,5] and Garret D. Stuber[1,2,4,6,*]

[1]Center for the Neurobiology of Addiction, Pain, and Emotion (NAPE), University of Washington, Seattle, WA 98195, USA
[2]Department of Anesthesiology and Pain Medicine, University of Washington, Seattle, WA 98195, USA
[3]Howard Hughes Medical Institute, University of Washington, Seattle, WA 98195, USA
[4]Department of Pharmacology, University of Washington, Seattle, WA 98195, USA
[5]Department of Neurobiology and Biophysics, University of Washington, Seattle, WA 98195, USA
[6]Lead contact
*Correspondence: gstuber@uw.edu
https://doi.org/10.1016/j.neuron.2025.04.024

SUMMARY

Opioid withdrawal is an intensively aversive experience and often drives relapse. The lateral septum (LS) is a forebrain structure that is important in aversion processing and has been linked to substance use disorders, but which LS cell types contribute to the maladaptive state of withdrawal is unknown. We used single-nucleus RNA sequencing to interrogate cell-type-specific gene expression changes induced by chronic morphine exposure and discovered that morphine globally disrupts LS cell types, but neurotensin-expressing neurons (LS-*Nts*) are selectively activated by naloxone. Using two-photon calcium imaging and *ex vivo* electrophysiology, we next demonstrate that LS-*Nts* neurons receive elevated glutamatergic drive in morphine-dependent mice and remain hyperactivated during withdrawal. Finally, we show that manipulating LS-*Nts* neurons during opioid withdrawal regulates pain coping and sociability. Together, these results suggest that LS-*Nts* neurons are a key neural substrate involved in opioid withdrawal and establish the LS as a crucial regulator of adaptive behaviors.

INTRODUCTION

Withdrawal from opioids is intense and highly aversive, which promotes drug seeking in persons with opioid use disorder (OUD). Anxiety, depression, and increased pain sensitivity are associated with opioid withdrawal, and this collective dysphoric state significantly contributes to relapse.[1,2] Throughout chronic opioid exposure, brain regions that normally support responses to natural rewards and threats undergo widespread neuroadaptations, ultimately shaping the brain in a way that perpetuates opioid misuse.[3] The lateral septum (LS) is a limbic forebrain structure that promotes reinforcement when electrically stimulated[4] and intense aversion when ablated.[5,6] That is, the LS gates both positive and negative motivation[7] and is thought to be a key structure involved in substance use disorders.[8–13] Indeed, rodents will self-administer opioids directly into the LS, which suggests that there is a subset of opioid-sensitive neurons in the LS that modulate positive reinforcement.[14–16] However, it remains unclear whether the LS confers withdrawal-induced dysphoria, despite its evident role in fear and stress processing.[7]

Although the LS is primarily a GABAergic hub, it is composed of neuronal subtypes expressing various neuropeptides, receptors, and transcription factors that contribute to cell type definition and function.[7,17,18] Activating *Crhr2*-expressing LS neurons produces aversion behavior,[19] while manipulating other putative LS subtypes does not seem to evoke the same aversion response,[20,21] further indicating that specific LS cell populations are specialized in processing positive and negative valence stimuli. Chronic opioids also impinge on both reward and aversion circuitry,[22] so uncovering distinct cell types in the LS is imperative for understanding its precise involvement in opioid dependence and withdrawal. While recent studies have targeted various neuropeptide- and receptor-expressing neurons, there is little consensus on LS cell types defined by their transcriptional heterogeneity. To this end, we used single-nucleus RNA sequencing (snRNA-seq) and developed a functional atlas to reveal which discrete LS cell populations are recruited during opioid withdrawal. Chronic morphine (Mor) produced global changes in genes underlying synaptic transmission and protein synthesis across the septum. By contrast, naloxone (Nal)-precipitated withdrawal most robustly

Please cite this article in press as: Simon et al., Opioid-driven disruption of the septum reveals a role for neurotensin-expressing neurons in withdrawal, Neuron (2025), https://doi.org/10.1016/j.neuron.2025.04.024

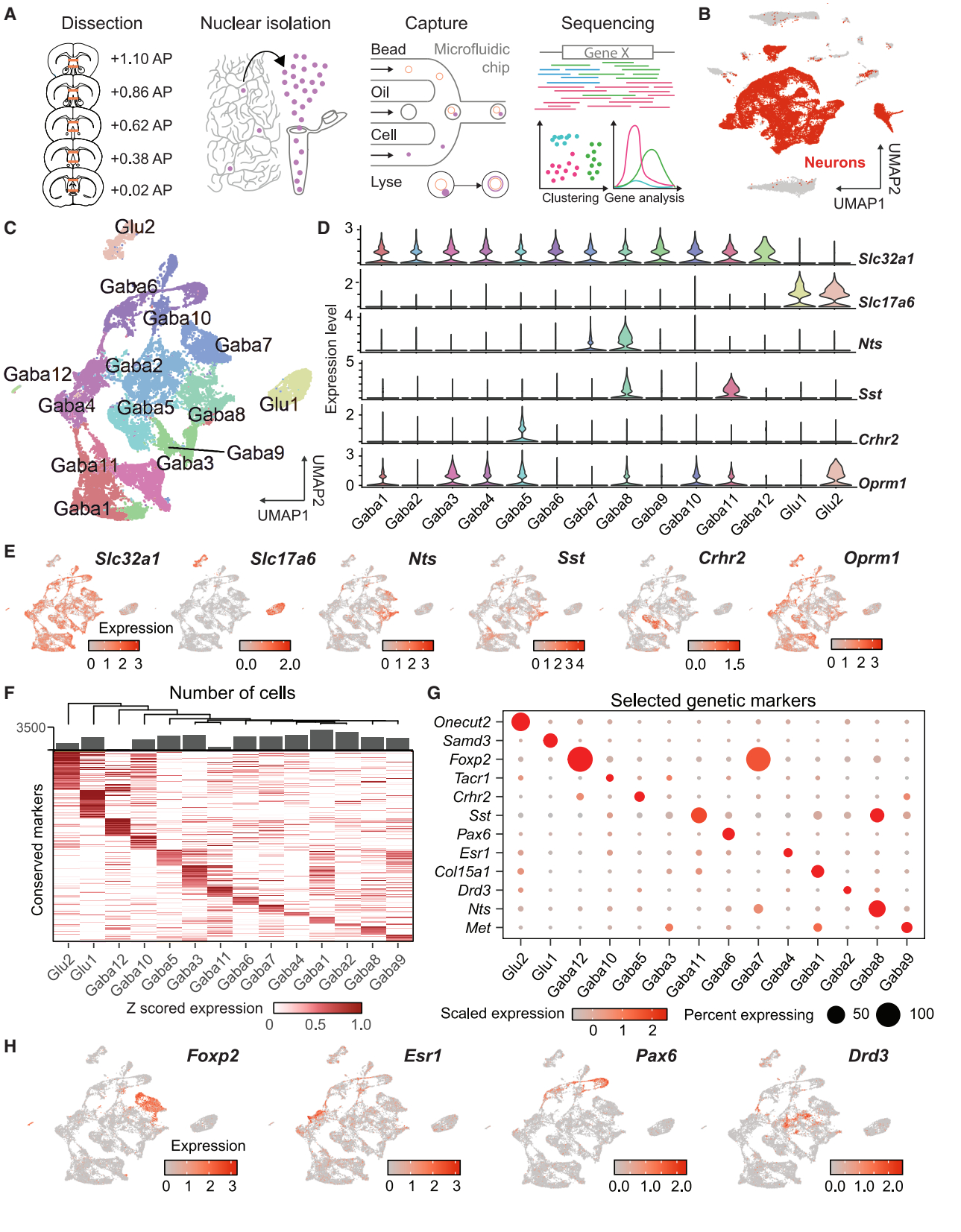

(legend on next page)

Please cite this article in press as: Simon et al., Opioid-driven disruption of the septum reveals a role for neurotensin-expressing neurons in withdrawal, Neuron (2025), https://doi.org/10.1016/j.neuron.2025.04.024

activated neurotensin-expressing LS neurons (LS-*Nts*). Further physiological characterization using two-photon imaging and *ex vivo* electrophysiology revealed that LS-*Nts* neurons remain hyperactivated during prolonged, spontaneous withdrawal. Finally, we demonstrated that bidirectional modulation of LS-*Nts* activity alters opioid withdrawal-induced pain sensitivity and social investigation.

RESULTS

snRNA-seq reveals a transcriptional atlas for cell types within the septal complex

To shed light on which septal cell types are preferentially disrupted during opioid dependence and withdrawal, we first identified discrete cell types in the septal complex defined by their single-cell gene expression. We collected septal tissue from ~8-week-old male and female C57BL/6J mice and isolated nuclei to generate snRNA-seq libraries (Figures 1A and S1A). In brief, we computationally removed doublets[23] and corrected for batch effects by utilizing an algorithm based on canonical correlation analysis (CCA)[24] and mutual nearest neighbors analysis.[25] Data dimensionality was reduced using principal-component analysis (PCA) based on the top 3,000 variable genes, which subsequently underwent graph-based clustering (Jaccard-Louvain) and was visualized using uniform manifold approximation and projection (UMAP). Of 53,188 total cells, 32,783 cells were retained as putative neurons based on the expression of *Stmn2* or *Thy1*, canonical neuronal markers typically used to subset neurons[26–28] (Figures 1B, S1B, and S1C). After removing potential contaminants and low-quality clusters, we retrieved a final total of 25,607 neurons. Neurons possessed a median unique molecular identifier (UMI) count of 6,075/cell and a median gene count of 2,757/cell, consistent with our previously published whole-cell transcriptomic datasets[29–31] (Figures S1D–S1F). Overall, our snRNA-seq data included high-quality neurons.

We identified 14 molecularly defined neuronal subtypes in the septum (2 glutamatergic and 12 GABAergic), which we determined by evaluating cluster stability over multiple clustering granularities (Figures 1C and S1G). Among these neurons, we found clusters that corresponded to previously identified LS cell types, including neurotensin- (*Nts*+; Gaba8), somatostatin- (*Sst*+; Gaba11), corticotropin-releasing hormone receptor 2- (*Crhr2*+; Gaba5), and dopamine receptor 3-expressing (*Drd3*+) neurons.[19–21,32–35] Although there was overlap between *Nts* and *Sst* expression (36.4% of *Nts*+ neurons co-express *Sst*), their respective major clusters were transcriptionally divergent (Gaba8 vs. Gaba11; Figure 1F). Mu opioid receptor (*Oprm1*) was also variably expressed throughout the septum (Figures 1D and 1E), indicating potential sensitivity to both opiates and endogenous opioids.[16] We next performed conserved marker analysis to identify genes that distinguish each cluster from one another (Figure 1F) and selected candidate molecular markers for each cluster based on the expression of each conserved gene (Figure 1G). Using this approach, we identified novel or understudied neuronal populations within the LS, including those expressing *Foxp2* (Gaba7/12), *Esr1* (Gaba4), *Met* (Gaba9), and *Pax6* (Gaba6). We next referred to other septum-specific sequencing datasets to verify the identity of our cell clusters. The putative LS markers *Trpc4*, *Dgkg*, and *Myob3*[36,37] were present in all cell clusters except for Gaba10, Glu1, and Glu2 (Figure S1H), and the medial septum (MS)-specific marker *Elavl2* was most highly expressed in Gaba10, Glu2, and Glu1 (Figure S1H). Because there was some non-specific expression of *Elavl2*, we subsequently cross-referenced our cell clusters with the Allen Brain Cell Atlas by mapping our cells onto their hierarchical cell cluster labels.[38] In brief, most neurons from our dataset mapped onto the Lateral septal complex (LSX) GABA class (~83%), indicating that our dissections and tissue preparations primarily contained LS neurons (Figure S1I). Gaba10 and Glu2 were likely the only MS-derived clusters in our dataset, whereas Gaba12 and Glu1 represented the septofimbrial nucleus of the septum (SFi). Interestingly, both LS- and SFi-residing cells comprised Gaba6, forming a hybrid cell cluster. All other clusters were likely derived from the LS (Figure S1I), consistent with our Allen Brain Cell Atlas mapping results.

Chronic Mor selectively disrupts the transcriptional landscape of the septum

Our snRNA-seq data contained experimental groups that we integrated into the same dataset (Figure 2A). To model opioid dependence, we used an escalating Mor paradigm because this approach has been shown to elicit robust, widespread physiological alterations that underlie drug-seeking behaviors.[39–41] Escalating Mor was given to wild-type (WT) C57BL/6J mice for 7 days (10–70 mg/kg), and on the final day, mice were sacrificed 1 h after their final dose (Mor group). Control mice were injected with saline (Sal) instead. To model precipitated opioid withdrawal, additional Mor subjects were given an injection of Nal (1 mg/kg) 1 h following their final Mor injection and were sacrificed 1 h later (Nal group). Nal-precipitated withdrawal produces behavioral phenotypes qualitatively consistent with spontaneous withdrawal during the prolonged absence of opioids.[3,40] After data integration, experimental groups were well represented across all cell types, and UMI and gene metrics were consistent across groups (Figures S2A–S2D; Table S1).

Figure 1. snRNA-seq reveals both canonical and undescribed cell populations within the septal complex

(A) Experimental schematic depicting the collection of septa from male and female C57BL/6J mice for snRNA-seq analysis.
(B) UMAP plot illustrating individual nuclei clustered according to their transcriptional similarities. Putative neurons are highlighted in red. *n* = 53,188 nuclei.
(C) UMAP plot of individual neurons clustered according to transcriptional similarities. *n* = 25,607 neurons across 14 bioinformatically defined clusters.
(D) Violin plots of the expression of established LS neuron markers.
(E) Feature plots indicating the expression of typical LS neuron markers across space.
(F) Heatmap of genes identified as conserved molecular markers for each neuronal cell type.
(G) Disc plot illustrating the prevalence of selected candidate markers for each cell cluster.
(H) Feature plots indicating the expression of selected candidate markers for Gaba7/12 (*Foxp2*+), Gaba4 (*Esr1*+), Gaba6 (*Pax6*+), and Gaba2 (*Drd3*+).

Please cite this article in press as: Simon et al., Opioid-driven disruption of the septum reveals a role for neurotensin-expressing neurons in withdrawal, Neuron (2025), https://doi.org/10.1016/j.neuron.2025.04.024

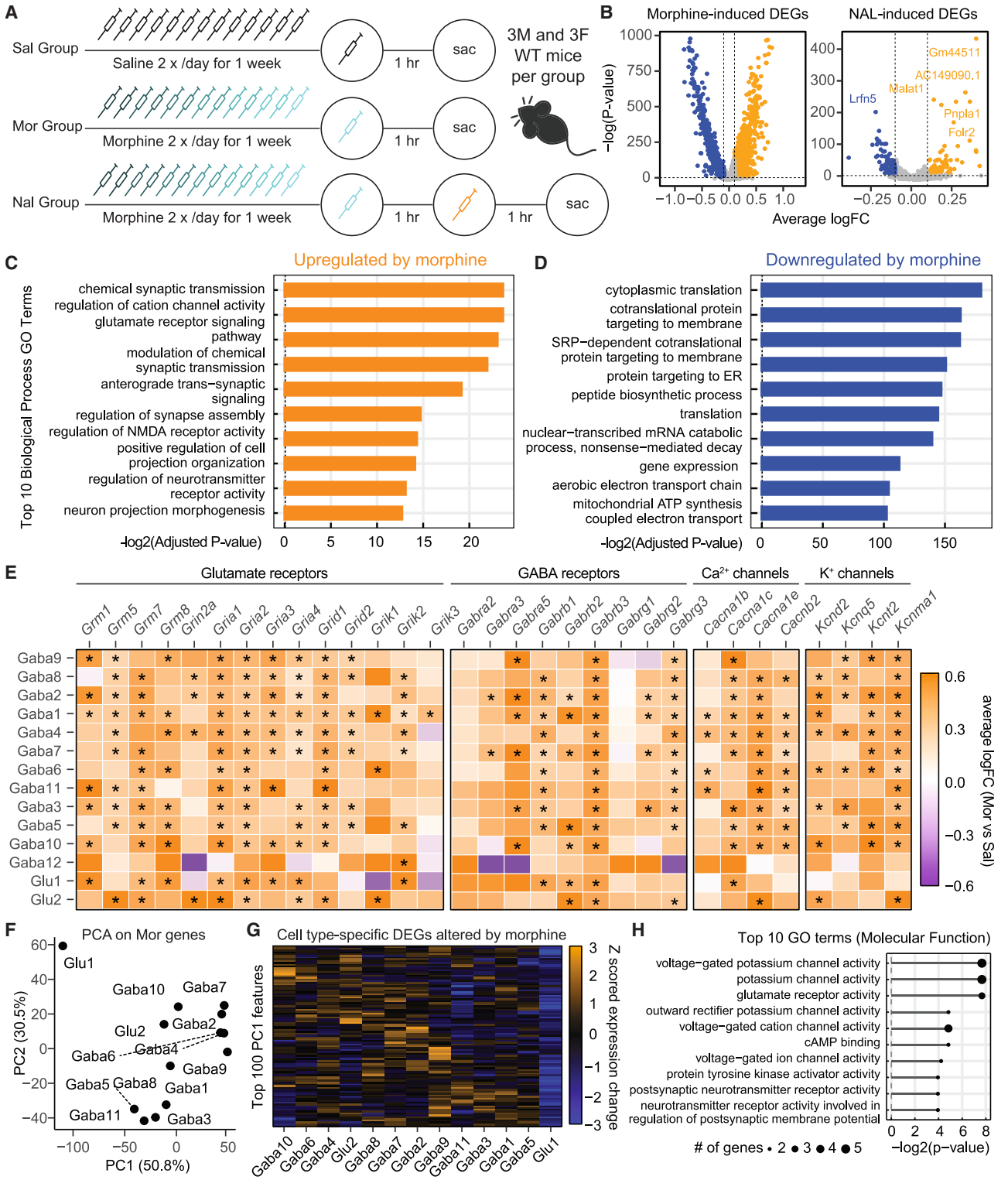

Figure 2. Chronic morphine selectively disrupts the transcriptional landscape of the septum

(A) Experimental schematic depicting C57BL/6J mice undergoing saline treatment (Sal), morphine escalation (Mor), or morphine escalation plus naloxone (Nal).

(B) Volcano plots showing DEGs induced by morphine (left) and by naloxone (right) across all cell clusters.

(C) Top 10 Gene Ontology (GO) terms (biological process) of genes upregulated by chronic morphine.

(D) Top 10 GO terms (biological process) of genes downregulated by chronic morphine.

(legend continued on next page)

Please cite this article in press as: Simon et al., Opioid-driven disruption of the septum reveals a role for neurotensin-expressing neurons in withdrawal, Neuron (2025), https://doi.org/10.1016/j.neuron.2025.04.024

We also added two additional experimental groups, but we were unable to reconcile sample gene expression differences because these samples were processed using different reagents and sequencing platforms (Figures S2E and S2F). However, we maintained these two groups in the base dataset for structural characterization only (see STAR Methods).

To identify widespread molecular changes induced by chronic opioids, we first ignored cell cluster labels and combined neurons from all clusters into single pools—one for Sal, one for Mor, and one for Nal. We then made pairwise comparisons between Sal vs. Mor and Mor vs. Nal to reveal differentially expressed genes (DEGs). Chronic Mor induced and repressed hundreds of DEGs in the septum (2,728 total). In comparison, Mor compared with Nal altered only 487 DEGs (Figure 2B). Processes involved in synaptic transmission, NMDA receptor activity, and regulation of neurotransmitter receptor activity (Gene Ontology [GO]: 0007268, 2000310, and 0099601) were upregulated (Figure 2C), whereas genes involved in translation, protein targeting to the endoplasmic reticulum, and gene expression (GO: 002181, 006412, 0045047, and 0010467) were downregulated by chronic Mor (Figure 2D). Mor-induced genes included glutamate receptors, GABA receptors, calcium channels, and potassium channels (Figure 2E), which were selectively upregulated across septal cell types. We next performed PCA on DEGs significantly altered by chronic Mor and determined which genes contributed most to cell type variability in DEG expression (Figures 2F and 2G). GO analysis on the top 100 features once again indicated that genes involved in potassium channel activity and glutamate receptor activity (GO: 0005249, 0005267, and 0008066) (Figure 2H) were potentially driving cell-type-specific responses to Mor. Together, our findings suggested that chronic Mor treatment may selectively alter synaptic transmission and membrane properties for different septal cell types.

Nts-expressing neurons in the septum are activated during Nal-precipitated withdrawal

To determine which specific LS cell types were recruited during Mor withdrawal, we next examined immediate early gene (IEG) expression, which is a molecular proxy for neuronal activity.[42–44] *Fos* was relatively depleted in our data with expression in only 3% of total neurons, but we detected other IEGs, such as *Arc* (5%), *Jund* (8%), and *Homer1* (47%) (Figure 3A). Therefore, we assessed a literature-based IEG inventory[27] across all our clusters. We first evaluated Nal-induced expression changes in "canonical" IEGs, such as *Fos*, *Arc*, *Egr1*, etc., by comparing Mor and Nal group-derived cells, but we found no statistically significant expression differences. We instead found other putative stimulus response genes that were significantly upregulated or downregulated (Figure 3B). Gaba8 (*Nts*+) neurons demonstrated the highest IEG induction (9 genes: *Gem*, *Pim1*, *Nptx2*, *Noct*, *Ackr4*, *Homer1*, *Rheb*, *Ncoa7*, and *Mbnl2*), followed by Gaba1, Gaba7, and Gaba2. To fully capture activation patterns, we next assessed a combined IEG metric of the genes that were significantly altered for every neuronal subtype and revealed that Gaba8 demonstrated the most robust change in the IEG profile (Figure 3C). Interestingly, we performed the same calculation for canonical IEGs and discovered that Gaba4 (*Esr1*+) neurons were the most enriched instead (Figure S3A).

Although some IEGs are well-known predictors of neuronal activity, there was variance in IEG expression based on cell cluster. We therefore corroborated our IEG analysis by evaluating Nal-induced DEG enrichment among each cell cluster, defined by the average number of upregulated and downregulated DEGs of 100 randomly sampled cells across 100 iterations. Gaba8 (*Nts*+) possessed the highest DEG enrichment induced by Nal compared with all other cell types (Figures 3D and 3E). We next utilized a random forest classifier to detect transcriptional changes across all cell clusters.[45] AUC scores indicated classifier accuracy, such that a higher score entails a higher degree of transcriptional change (see STAR Methods). Not only were Gaba8 neurons among the most transcriptionally altered by chronic Mor, but they were also ranked the second most perturbed by Nal (Figures S3C and S3D). Because the Mor vs. Nal AUC scores were close to 0.50, we also statistically tested for the differences in AUC score distributions to delineate between Nal-perturbed and Nal-non-perturbed clusters. Although AUC scores were close to chance, they were significantly elevated in some clusters, notably Gaba8 (*Nts*+), suggesting that the classifier could distinguish between Mor and Nal within specific neuronal subtypes (Figure S3E).

Because *Oprm1* was expressed throughout the septum (Figure 1D), it was possible that *Oprm1* expression is linked to septal activation induced by opioid withdrawal. However, there was no correlation between mean *Oprm1* expression and the Nal-induced DEG score for each cell type (Figure S3G). Because Nal can also bind to kappa and delta opioid receptors,[46] we also examined *Oprk1* or *Oprd1* expression and found that there was a moderate and significant correlation between *Oprk1* expression and the Nal DEG enrichment score across cell clusters (Figures S3G and S3H). Because very few cells express *Oprk1* in our dataset (e.g., 3.4% of Gaba8) (Figures S3G and S3H), we sought other potential correlates for DEG enrichment. We subsequently discovered a strong, significant relationship between Nal-induced transcriptional changes and *Nts* expression in neuron clusters (Figure 3F). Although Gaba8 possessed the highest *Nts* expression, other clusters (e.g., LS-*Foxp2*) also expressed *Nts*. We next determined what genes distinguish *Nts*+ from *Nts*− neurons, agnostic to cell cluster. Genes involved in chemical synaptic transmission (GO: 0097268) and regulation of neurotransmitter receptor activity (GO: 0099601), specifically genes encoding receptors for catecholaminergic signaling like *Drd2* and *Adra1a*, were enriched in *Nts*+ neurons (Figures 3G, 3H, and S3I).

From this analysis, we reasoned that LS-*Nts* neurons could be further divided into subtypes that are modulated by diverse

(E) Heatmap illustrating the average logFC of Mor vs. Sal for different gene classes. "*" indicates significance ($p < 0.05$; Wilcoxon rank-sum test followed by Benjamini-Hochberg post hoc comparison correction).
(F) PCA of the logFC expression of DEGs between Sal and Mor.
(G) Heatmap of the top 100 features identified in PC1 across all cell types.
(H) Top 10 GO terms (molecular function) identified from the top 100 features.

Please cite this article in press as: Simon et al., Opioid-driven disruption of the septum reveals a role for neurotensin-expressing neurons in withdrawal, Neuron (2025), https://doi.org/10.1016/j.neuron.2025.04.024

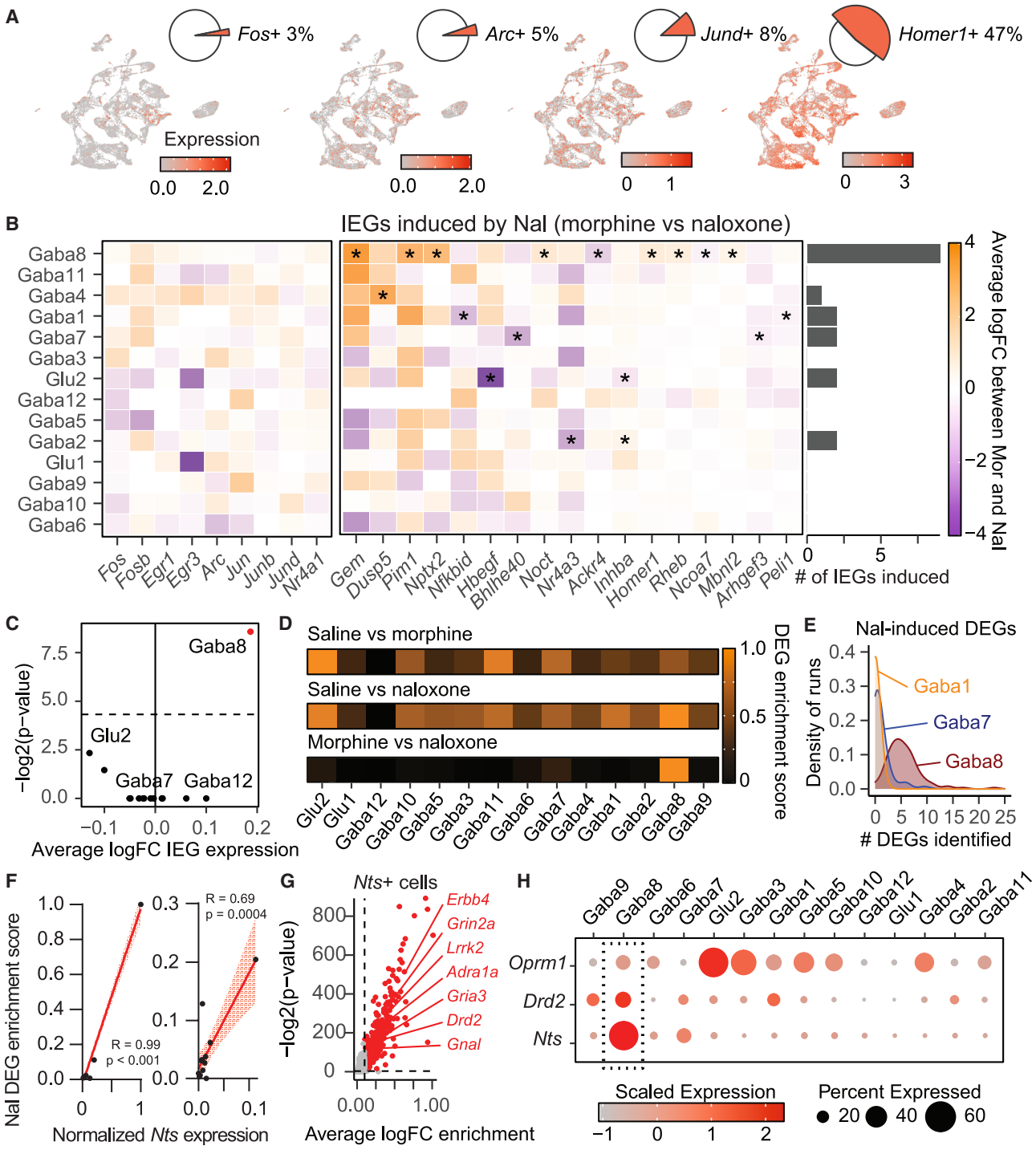

Figure 3. *Nts*-expressing neurons in the septum are recruited during Nal-precipitated withdrawal

(A) Feature plots of IEGs *Fos*, *Arc*, and *Homer1*. Insets, proportion of neurons expressing each IEG.

(B) Heatmap of Nal-induced IEG expression. Left, classic IEGs; middle, any "extended" IEG that was significantly altered in any cell type; right, number of IEGs induced within each cluster. "*" indicates significance ($p < 0.05$; Wilcoxon rank-sum test followed by Benjamini-Hochberg post hoc correction).

(C) Average logFC expression difference between Mor and Nal of all statistically significantly altered IEGs for each cell cluster. Wilcoxon rank-sum test followed by Bonferroni's post hoc correction. Red indicates statistically significant clusters.

(D) Normalized DEG enrichment scores across cell types for each condition comparison (Sal vs. Mor, Sal vs. Nal, and Mor vs. Nal).

(legend continued on next page)

Please cite this article in press as: Simon et al., Opioid-driven disruption of the septum reveals a role for neurotensin-expressing neurons in withdrawal, Neuron (2025), https://doi.org/10.1016/j.neuron.2025.04.024

inputs. We identified receptor-coding genes that are enriched in *Nts*+ cells, including *Glp2r*, *Ntrk2*, and *Adrb1*, in addition to *Drd2* and *Adra1a*. *Crhr2* and *Met* were also included in our analysis, as a small percentage of *Nts*+ cells also expressed these receptors that mark other LS neuronal populations. To assess whether subtypes expressing each of these receptors are transcriptionally altered following Nal-precipitated withdrawal, we first subset *Nts*+ neurons that express at least one copy of a given gene (i.e., one copy of *Drd2* defines that cell as *Drd2*+). We defined subtypes as nonexclusive, as there was overlapping expression among each of these receptors, and we calculated an IEG score using the seven IEGs that showed a statistically significant upregulation in the Gaba8 cluster (Figure 3C). From this analysis, we found that *Nts*+/*Drd2*+ and *Nts*+/*Ntrk2*+ cells demonstrated statistically significant increases in IEG scores (Figure S3J). Given these results, precipitated withdrawal likely differentially activates LS-*Nts* subpopulations in an input-driven manner.

Discrete LS cell types are organized as a gradient across the medial-lateral and dorsal-ventral axes

Although our snRNA-seq data implicated Gaba8 (*Nts*+) neurons as the predominant cell population disrupted during Mor withdrawal, we sought to verify our findings in tissue space. We performed hybridization chain reaction (HCR), which is a highly multiplexed *in situ* hybridization technique that measures many genes simultaneously through sequential rounds of hybridization, amplification, imaging, and probe digestion on the same tissue.[47,48] We used septal tissue from 8 naive WT mice with 15 DNA probes designed to target the following genes: *Nts*, *Drd2*, *Drd3*, *Sst*, *Crhr2*, *Tacr1*, *Foxp2*, *Esr1*, *Met*, *Samd3*, *Col15a1*, *Slc32a1*, *Pax6*, *Onecut2*, and *Slc17a6* (Figures 4A and 4B). Twelve of these genes were molecular markers for snRNA-seq-identified cell clusters. Once images were registered onto the same plane, we plotted spatial maps based on the normalized density of cells positive for each gene (Figure 4C). Each molecularly defined LS cell type was organized as non-discrete laminae that extend from rostral to caudal aspects of the tissue, which likely arise during the "inside-out" development of the septal complex.[49] *Col15a1*+ and *Onecut2*+ were the densest and most abundant cells, whereas *Esr1*+ and *Pax6*+ were the rarest. Incidentally, there was a high degree of overlap among cell populations in the rostral aspects of the LS but to a lesser degree in caudal regions (Figures 4D and S4A).

To evaluate the congruency between snRNA-seq and HCR, we clustered cells based on HCR gene expression data (Figures S4B and S4C). The correlation between the abundance of cells expressing each gene in the snRNA-seq and HCR datasets was robust and statistically significant. This correlation was driven primarily by *Slc32a1* expression, but this relationship ultimately extended to a cluster-by-cluster basis as well (Figure 4E). Therefore, despite differences in sampling biases of the two techniques, the relative distribution of each cell type was consistent across the two datasets. We next inferred where each snRNA-seq cell cluster may anatomically reside within the septal complex. Gaba2 (LS-*Drd3*), Gaba4 (LS-*Esr1*), Gaba5 (LS-*Crhr2*), Gaba7 (LS-*Foxp2*), Gaba8 (LS-*Nts*), and Gaba11 (LS-*Sst*) comprised a large portion of the intermediate LS. As expected, Glu2 and Gaba10 represented the MS, and Glu1 likely resided in the SFi This is consistent with our predictions from our snRNA-seq (Figures S1H and S1I).

We also verified that Nal induced IEG expression in LS-*Nts* neurons *in situ*. A new cohort of mice underwent Mor escalation, Mor withdrawal (Nal), and repeated Sal injections and were sacrificed 1 h after injection completion. We probed for *Fos* expression in both LS-*Nts* and LS-*Met* cells, as both were implicated as Nal-responsive cell types in our snRNA-seq data (Figure 4F). Here, we limited our *in situ* experiment to measuring *Fos* due to its established role in neuronal activity.[50] While both LS-*Nts* (exclusive of *Met*) and LS-*Met* (exclusive of *Nts*) demonstrated Nal-induced *Fos* expression, LS neurons expressing both *Nts* and *Met* showed the highest *Fos* induction during precipitated withdrawal (Figures 4G and 4H). Incidentally, cells negative for both were depleted for *Fos* (Figures S4E–S4G). We found that neurons co-expressing *Nts* and *Met* resided in the intermediate aspect of the LS (LSi) (Figures S4H and S4I). We also considered that Nal may simply increase *Fos* expression in LS-*Nts*-*Met* neurons regardless of opioid history. To examine this possibility, we conducted an acute exposure experiment in which a new cohort of mice received a single injection of 10 mg/kg Mor, 1 mg/kg Nal, or Sal and were sacrificed 1 h after injection. We found that Nal did not alter *Fos* expression in LS neurons co-expressing *Nts* and *Met* of opioid-naive mice (Figures S4J–S4M), indicating that Nal may selectively increase the activity of LS-*Nts*-*Met* neurons following Mor treatment. Together, our snRNA-seq and HCR analyses revealed that Nal restored the activity of LSi-localized LS-*Nts* neurons to baseline in opioid-dependent mice.

Opioid withdrawal elevates LS-*Nts* activity *in vivo*

Opioid withdrawal disrupts emotional regulation, producing a multifaceted dysphoric state that includes both anhedonia and hypersensitivity to fear and stress.[51,52] Therefore, we next sought to reveal whether opioid exposure and withdrawal alter LS-*Nts* responsivity to rewarding and aversive stimuli *in vivo*. To this end, we used two-photon imaging in awake, behaving mice, which allowed us to track how the activity of single neurons is altered during the emergence of opioid dependence. We injected *Nts*-Cre mice with AAVDJ-EF1a-DIO-GCaMP6s unilaterally in the LSi, followed by a GRIN lens implantation directly above the same site (Figure 5A). Once mice were habituated to head-fixation, we first imaged mice as drug-naive to establish baseline calcium dynamics for LS-*Nts* neurons. LS-*Nts* neurons expressing GCaMP6s were spontaneously active *in vivo* (Figures 5B, S5A, and S5B). We then exposed mice to interleaved presentations of 10% sucrose (rewarding; 80% of trials) and 20 psi air puffs (mildly aversive; 20% of trials) to evaluate

(E) Density histogram indicating the frequency of the number of DEGs identified for Gaba7, Gaba8, and Glu2 across 100 runs.
(F) The relationship between normalized *Nts* expression (*x* axis) and Nal DEG enrichment (*y* axis). Left, including Gaba8. Right, excluding Gaba8.
(G) Scatterplot illustrating the genes that were significantly enriched in *Nts*+ cells vs. *Nts*− cells.
(H) Disc plot illustrating *Oprm1*, *Drd2*, *Adra1a*, and *Nts* expression.

Please cite this article in press as: Simon et al., Opioid-driven disruption of the septum reveals a role for neurotensin-expressing neurons in withdrawal, Neuron (2025), https://doi.org/10.1016/j.neuron.2025.04.024

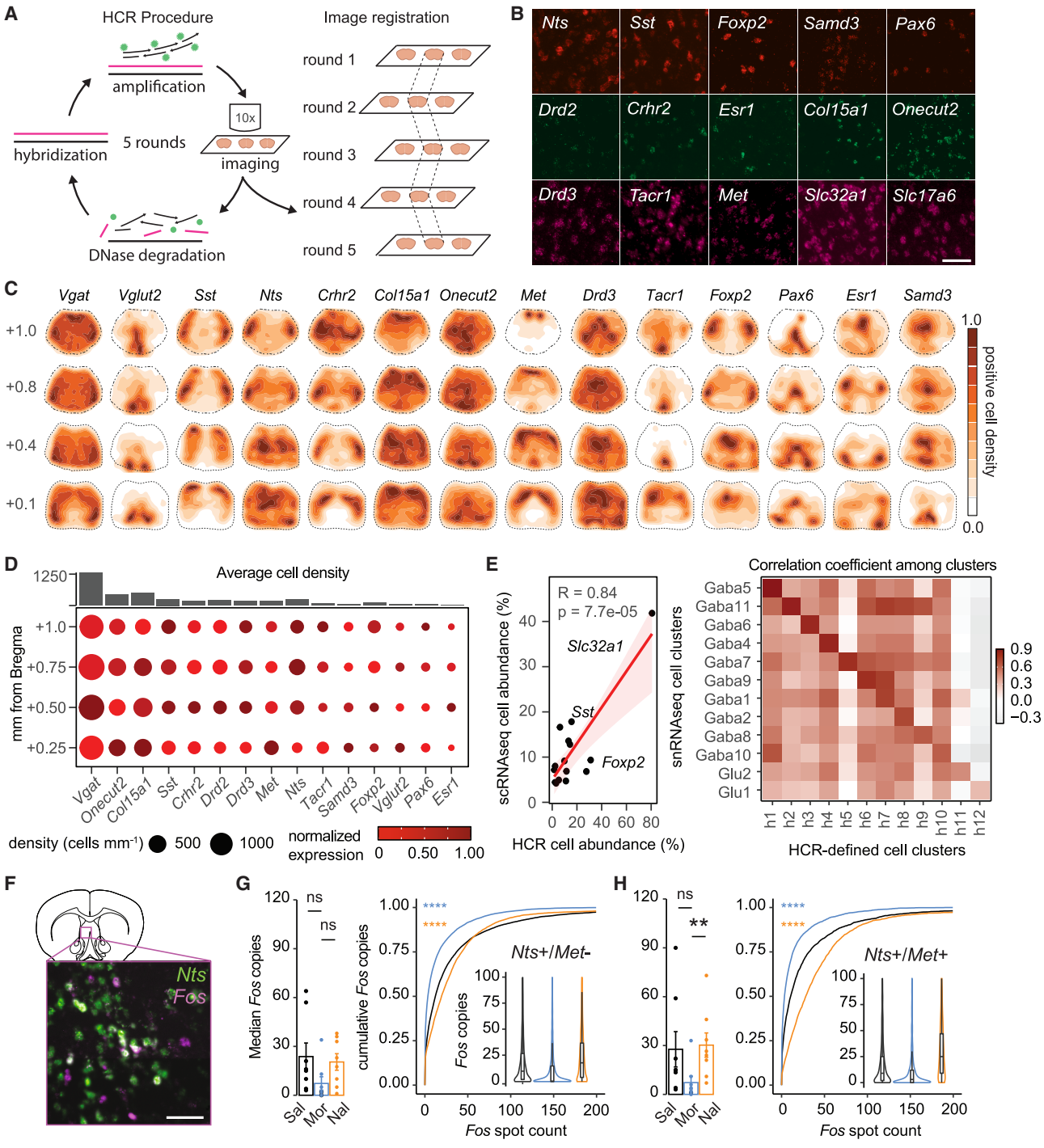

Figure 4. The septal complex possesses gradient-like laminae that may be selectively recruited during opioid withdrawal

(A) Experimental schematic. Septal tissue from 4 male and 4 female C57BL/6J mice were stained for each candidate marker identified from snRNA-seq using HCR.

(B) Representative images for each probe. Scale bar, 50 μm.

(C) Spatial density plots for each gene from all animals collapsed into one dataset.

(D) Disc plot of HCR gene expression across the AP axis of the septum.

(E) Left, correlation between the abundance of cell types identified in snRNA-seq vs. HCR. Right, correlation among clusters defined by snRNA-seq (*y* axis) and HCR (*x* axis).

(F) Representative images of *Nts* and *Fos* expression *in situ*. Scale bar, 100 μm.

(legend continued on next page)

Please cite this article in press as: Simon et al., Opioid-driven disruption of the septum reveals a role for neurotensin-expressing neurons in withdrawal, Neuron (2025), https://doi.org/10.1016/j.neuron.2025.04.024

how innately positive and negative valenced stimuli modulate LS-*Nts* activity. Mice were then subsequently split into either Sal-treated or Mor-treated groups. Neuronal activity was recorded every other day during our Mor escalation protocol (Figure 5C; days 2, 4, and 6). Each imaging session occurred before mice received any Sal or Mor for that day, as we found that high doses of Mor suppressed appetitive licking for several hours. LS-*Nts* neurons were responsive to both air puffs and sucrose (Figure 5D), and Sal and Mor neurons were not significantly different in their responsivity to either stimulus at baseline. While opioid exposure did not influence response magnitude to air puffs and sucrose, it reduced the proportion of cells responding to sucrose and not air puffs on days 2 and 4 (Figures S5C and S5D).

To examine whether Nal activates LS-*Nts* neurons *in vivo*, we gave mice their final Sal or Mor injection on day 7 and recorded LS-*Nts* activity ~30 min following treatment. Afterward, Sal and Mor mice were injected with Nal and re-imaged ~30 min following Nal treatment. We found that acute Mor exposure blunted both air puff- and sucrose-evoked responses from LS-*Nts* neurons (Figures 5E and 5F). Interestingly, Nal treatment rapidly reversed the influence of Mor on LS-*Nts* neurons in opioid-dependent mice, allowing these neurons to recover responses to both sucrose and air puffs (Figure 5F). Sal neurons, by contrast, were mildly but not significantly suppressed following Nal treatment. While it was evident that Nal modulated LS-*Nts* activity, it was unclear whether LS-*Nts* activity changes during withdrawal were transient or prolonged. To address this, we re-imaged mice 1 week following the completion of Mor injections. We found that although air puff and sucrose-evoked responses were minimally different between Sal and Mor neurons at 1 week of spontaneous withdrawal (Figure S5E), neurons from Mor-treated mice showed higher and longer-lasting calcium peaks compared with neurons recorded in Sal-treated mice (Figures 5G–5I). LS-*Nts* neurons may possess constitutively higher spontaneous activity during sustained abstinence from Mor, indicating LS-*Nts* neurons as a potential regulator of behavioral dysfunction during opioid withdrawal.

Glutamatergic drive is enhanced at LS-*Nts* neurons during opioid withdrawal

Because our snRNA-seq data indicated that chronic Mor upregulated glutamate receptor gene expression in LS-*Nts* neurons (Figure 2E), we reasoned that these neurons may undergo excitatory synaptic strengthening during Mor exposure. In the absence of Mor, LS-*Nts* neurons may then become hyperactivated due to increased glutamatergic drive. Therefore, we next sought to determine whether LS-*Nts* displayed alterations in synaptic transmission using *ex vivo* electrophysiology. To label LS-*Nts* neurons for identification during electrophysiology experiments, we injected AAV5-hSyn-DIO-eYFP bilaterally into the LS of *Nts*-Cre mice (Figure 6A). To assess specificity, we also labeled *Sst*-expressing neurons in the dorsocadual aspect of the LS via injection of the same virus into *Sst*-Cre mice, as we expected there to be little overlap between LS-*Nts* and caudal LS-*Sst* neurons. 2 weeks later, mice underwent the same Mor escalation paradigm (Mor) or received Sal. All mice received Nal. 6–10 days later, brain slices were collected for synaptic physiology measurements (Figure 6A). Miniature excitatory and inhibitory postsynaptic currents (mEPSCs and mIPSCs) were recorded in a whole-cell configuration with membrane voltage clamped at −70 mV for mEPSCs and +10 mV for mIPSCs (Figure 6B). When possible, both measurements were collected from the same cell. LS-*Nts* neurons from mice that underwent Mor treatment and withdrawal showed increased mEPSC frequency (Figures 6C and 6D) and amplitude (Figure 6E) compared with Sal-treated mice, suggesting that chronic Mor and withdrawal increase excitatory synaptic strength at these neurons. Overall inhibitory synaptic strength at LS-*Nts* neurons was unaffected by Mor, as mIPSC frequency and amplitude at LS-*Nts* neurons remained unchanged in Mor-treated mice (Figures 6F–6H). Interestingly, LS-*Sst* neurons did not exhibit any change in mEPSCs (Figures 6I–6K) or mIPSCs (Figures 6L–6N), highlighting that the effects observed in LS-*Nts* neurons do not reflect global changes in synaptic strength in LS. Overall, our *ex vivo* electrophysiology experiments demonstrated that opioid dependence and withdrawal likely drive a cell-type-specific enhancement of glutamatergic synaptic strength at LS-*Nts* neurons.

Silencing LS-*Nts* neurons exacerbates withdrawal-induced pain coping and triggers sexually dimorphic alterations in sociability

Elevated LS-*Nts* activity following opioid abstinence might contribute to maladaptive behaviors associated with opioid withdrawal. To test this, we used genetically encoded tetanus toxin light chain (TetTox) to silence these neurons. TetTox disrupts vesicle release machinery and prevents neurotransmission from treated neurons.[53] Incidentally, TetTox silencing has been functionally validated in another study examining LS-*Nts* neurons in feeding.[32] After injecting 14 animals with AAVDJ-EF1a-DIO-TetTox-GFP (TetTox group) and 12 animals with AAV5-EF1a-DIO-eYFP (control group), we waited 8–10 weeks for viral expression and performed a battery of 6 behavioral tests over a 2-month period (Figures 7A and 7B). Following baseline testing, control and TetTox mice underwent Mor escalation and precipitated withdrawal. We then measured behavioral changes during 1–2 and 4–5 weeks of Mor withdrawal. Using this method, we assessed how chronic loss of LS-*Nts* function influences the emergence of withdrawal phenotypes.

We first evaluated feeding behaviors, as previously published studies showed that chemogenetic increases of Gi signaling in LS-*Nts* neurons promote overeating.[21,32] Here, we found that silencing LS-*Nts* neurons modulates food consumption but not in the context of opioid withdrawal (Figures S6A–S6D). Next,

(G) Cells positive for *Nts* only. Sal vs. Mor: median copies per section ($p = 1$); median copy difference ($p = 1.05 \times 10^{-10}$). Mor vs. Nal: median copies per section ($p = 0.0897$), median copy difference ($p = 4.28 \times 10^{-5}$).
(H) *Nts*+ and *Met*+ cells. Sal vs. Mor: median copies per section ($p = 0.551$); median copy difference ($p = 7.58 \times 10^{-10}$). Mor vs. Nal: median copies per section ($p = 0.0181$); median copy difference ($p = 1.71 \times 10^{-13}$). All data are represented as mean ± SEM. #$p < 0.1$, *$p < 0.05$, **$p < 0.01$, ***$p < 0.001$, ***$p < 0.001$, ****$p < 0.0001$.

Please cite this article in press as: Simon et al., Opioid-driven disruption of the septum reveals a role for neurotensin-expressing neurons in withdrawal, Neuron (2025), https://doi.org/10.1016/j.neuron.2025.04.024

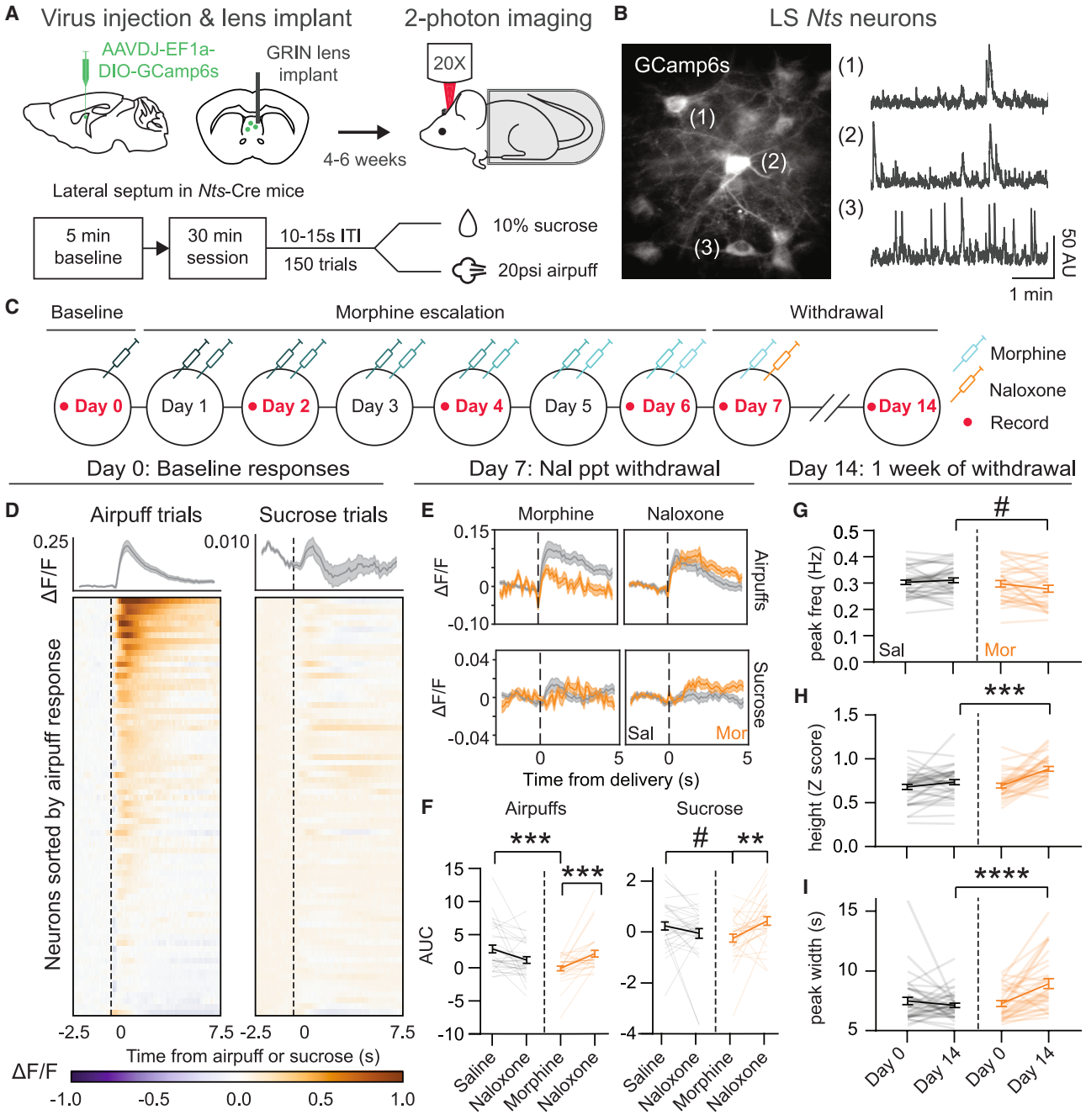

Figure 5. Opioid withdrawal elevates LS-*Nts* activity *in vivo*

(A) Experimental schematic. 4 male and 2 female *Nts*-Cre mice were injected with AAVDJ-EF1a-DIO-GCaMP6s and implanted with a GRIN lens for two-photon imaging.

(B) Left, sample mean image of GCaMP6s expression in LS-*Nts* neurons from a representative animal. Right, sample raw fluorescence traces of three representative neurons.

(C) Experimental timeline. Baseline data were taken prior to Sal or escalating Mor injections.

(D) LS-*Nts* activity evoked by air puffs and sucrose presentations in one representative mouse on day 0. Top, lick rate aligned to air puff or sucrose presentations. Bottom, peri-event time histograms of neuronal responses to air puffs (left) and sucrose (right). $n = 79$ cells.

(E) Mean Nal-induced responses of Sal-treated ($n = 33$) and Mor-treated ($n = 32$) cells to air puffs (top) and sucrose (bottom).

(F) AUC measurements for air puff-evoked (left) and sucrose-evoked (right) responses of Sal- and Mor-treated cells before and after Nal.

(G–I) Spontaneous activity analysis of Sal-treated and Mor-treated cells on day 14, including (G) peak frequency, (H) peak amplitude, and (I) peak width. All statistics are reported in Table S2. All data are represented as mean ± SEM. #$p < 0.1$, *$p < 0.05$, **$p < 0.01$, ***$p < 0.001$, ***$p < 0.001$, ****$p < 0.0001$.

Please cite this article in press as: Simon et al., Opioid-driven disruption of the septum reveals a role for neurotensin-expressing neurons in withdrawal, Neuron (2025), https://doi.org/10.1016/j.neuron.2025.04.024

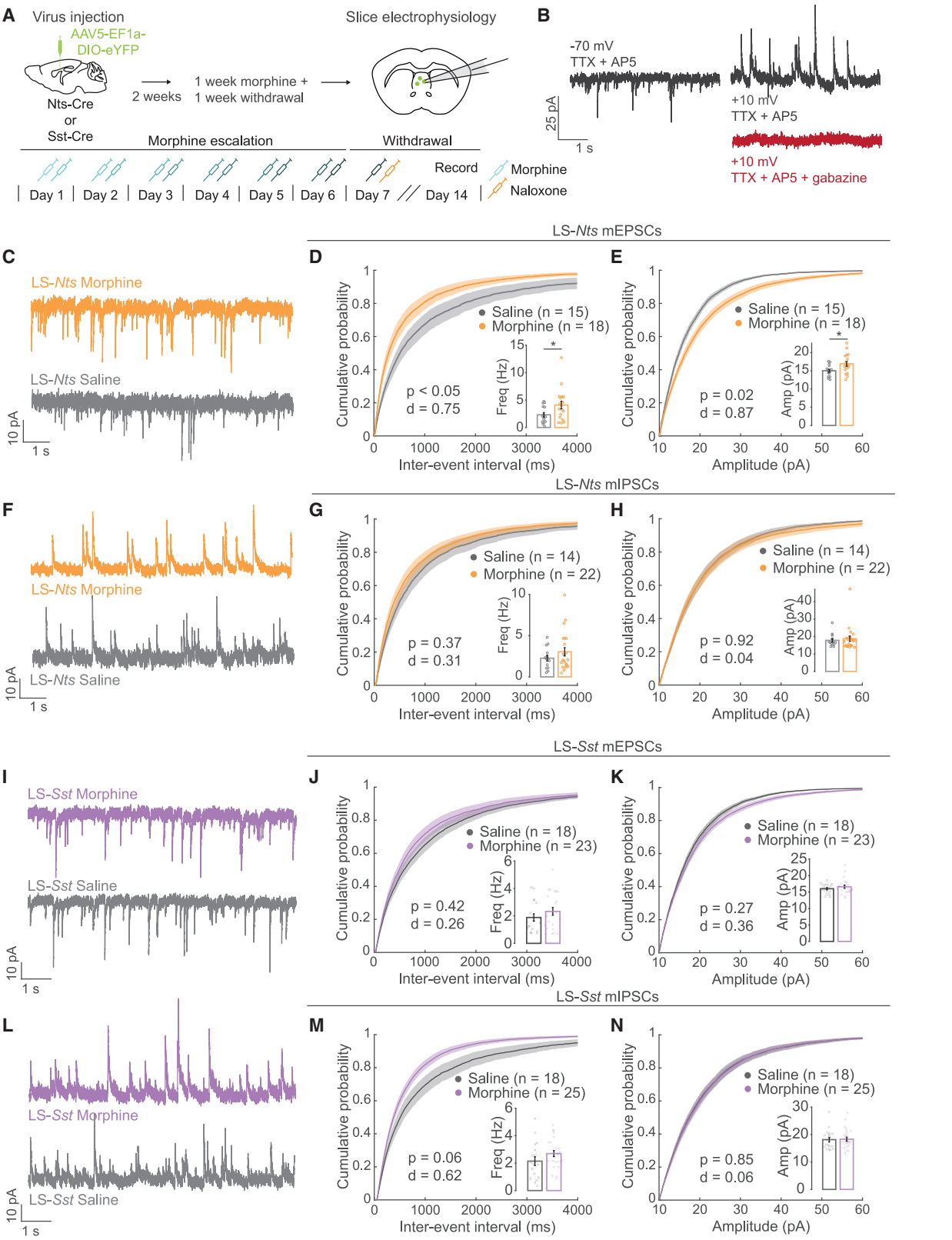

(legend on next page)

Please cite this article in press as: Simon et al., Opioid-driven disruption of the septum reveals a role for neurotensin-expressing neurons in withdrawal, Neuron (2025), https://doi.org/10.1016/j.neuron.2025.04.024

we tested whether manipulating LS-*Nts* activity altered withdrawal-associated behaviors. Silencing LS-*Nts* neurons did not influence somatic signs of withdrawal (fecal boli and spontaneous jumping[54–56]), indicating that LS-*Nts* are not necessary for the expression of these withdrawal signs (Figure 7C). Approximately 24 h following Nal, we next tested whether mice experienced hyperalgesia via a hot plate assay and found that TetTox mice licked their hind paw or jumped sooner than controls. TetTox mice also jumped more frequently in the hotplate test at 1d following Nal treatment, suggesting opioid withdrawal decreased their pain threshold (Figure 7D). It was possible that silencing LS-*Nts* elevated gross locomotion, but spontaneous movement in an open field was slightly reduced in TetTox mice (Figures 7E and S6E). LS-*Nts* does not seem to influence anxiety-like behaviors during opioid withdrawal, as there was no difference in open field center time (Figure S6F) or elevated plus maze performance (Figures S6G and S6H).

Opioid withdrawal triggers severe social deficits in humans, including social isolation and aggression, which can perpetuate OUD as individuals are less likely to receive the support necessary to abstain from drug misuse.[57–59] The LS is well-implicated in social behaviors, including social interaction, aggression, mating, and pup-rearing,[60] but it is unknown whether LS-*Nts* neurons play a role in withdrawal-induced social deficits. To test this, TetTox and control mice were placed within a 3-chamber apparatus, in which they were presented with an unfamiliar same-sex mouse and an unfamiliar object. At 1 week of opioid withdrawal, TetTox mice spent less time in the mouse-paired chamber than controls (Figure 7F), indicating that LS-*Nts* activity influences social preference during early opioid withdrawal. The 3-chamber assay does not allow naturalistic social interactions, so we next performed a resident intruder (RI) task, in which a younger, same-sex albino mouse was placed into the resident mouse's home cage. Recent evidence suggests that LS-*Nts* neurons modulate social approach in male—but not female—mice,[61] prompting us to examine sex-specific effects in the RI task. TetTox treatment increased the frequency of nose-to-nose interactions in male mice, indicating that silencing LS-*Nts* produces a prosocial state in males (Figure 7G). To assess whether optogenetic activation of LS-*Nts* neurons suppresses social interaction, we next prepared a cohort of male mice that received bilateral optical fiber implants and injections of AAV5-Ef1a-DIO-ChR2-eYFP (ChR2) or AAV5-Ef1a-DIO-eYFP (control) into the LS (Figure 7H). These mice underwent a 12 min RI session prior to and 1 week following Nal-precipitated withdrawal, during which they received interleaved presentations of blue light (Figure 7I). Optogenetic activation of LS-*Nts* neurons reduced nose-to-nose interactions with intruder mice during opioid withdrawal (Figures 7J and 7K). Further, optically activating LS-*Nts* neurons decreased pain expression (Figures S6I–S6K), demonstrating that LS-*Nts* neurons can bidirectionally regulate social and pain-related behaviors during opioid withdrawal. Finally, we evaluated LS-*Nts* projection targets and found that the retrohippocampal area, lateral hypothalamus (LH), nucleus accumbens, medial and lateral preoptic areas, and the bed nucleus of the stria terminalis were among the top targets of LS-*Nts* neurons (Figure S7), indicating that LS-*Nts* projection diversity may underlie this population's role in adaptive behaviors.

DISCUSSION

Opioid withdrawal is a powerful motivator for relapse, highlighting the importance of understanding how aversion circuitry in the brain is disrupted by chronic opioid exposure. We chose to study the LS because of its role in mediating both hedonic and aversion responses, which are disrupted during withdrawal. Chronic opioid exposure disrupts synaptic connectivity and structural plasticity within neural circuitry supporting reward and aversion processing,[62,63] molding a system that perpetuates drug craving and relapse vulnerability. Although the cell types we delineated in this paper are largely consistent with other studies[36,37,64] that performed transcriptional characterization of the LS, there was no resource for opioid-driven transcriptional adaptations in the septum, which can provide a guide for which cell types are most pertinent to study in the context of limbic dysfunction in OUD. We utilized our snRNA-seq guide to establish LS-*Nts* neurons as a novel neural substrate both perturbed by opioid dependence and selectively disrupted by precipitated withdrawal, and we ultimately show that these neurons modulate behavioral responding during protracted opioid withdrawal.

Developing a functional atlas of the LS

LS neurons receive afferents from hippocampal subregions in a spatially deterministic manner and may be differentially recruited

Figure 6. Mor treatment and withdrawal alter excitatory, but not inhibitory, synaptic strength at LS-*Nts* neurons

(A) Schematic for viral labeling LS-*Nts* neurons and experimental timeline.

(B) Example whole-cell, voltage-clamp traces from an LS-*Nts* neuron. mEPSCs were measured at −70 mV (left), and mIPSCs were measured at +10 mV (right). Currents at +10 mV were abolished by gabazine (bottom).

(C) Example traces of mEPSCs in LS-*Nts* neurons.

(D and E) Cumulative probability of inter-event intervals (D) and amplitudes (E) for LS-*Nts* mEPSCs. Insets: median frequency (D) and amplitude (E) of LS-*Nts* mEPSCs.

(F) Example traces of mIPSCs in LS-*Nts* neurons.

(G and H) Cumulative probability of inter-event intervals (G) and amplitudes (H) for LS-*Nts* mIPSCs. Insets: median frequency (G) and amplitude (H) of LS-*Nts* mIPSCs.

(I) Example traces of LS-*Sst* mEPSCs.

(J and K) Cumulative probability of inter-event intervals (J) and amplitudes (K) for LS-*Sst* mEPSCs. Insets: median frequency (J) and amplitude (K) of LS-*Sst* mEPSCs.

(L) Example traces of LS-*Sst* mIPSCs.

(M and N) Cumulative probability of inter-event intervals (M) and amplitudes (N) for LS-*Sst* mIPSCs. Insets: median frequency (M) and amplitude (N) of LS-*Sst* mIPSCs. All statistics are reported in Table S2. All data are represented as mean ± SEM. #$p < 0.1$, *$p < 0.05$, **$p < 0.01$, ***$p < 0.001$, ***$p < 0.001$, ****$p < 0.0001$.

Please cite this article in press as: Simon et al., Opioid-driven disruption of the septum reveals a role for neurotensin-expressing neurons in withdrawal, Neuron (2025), https://doi.org/10.1016/j.neuron.2025.04.024

CellPress

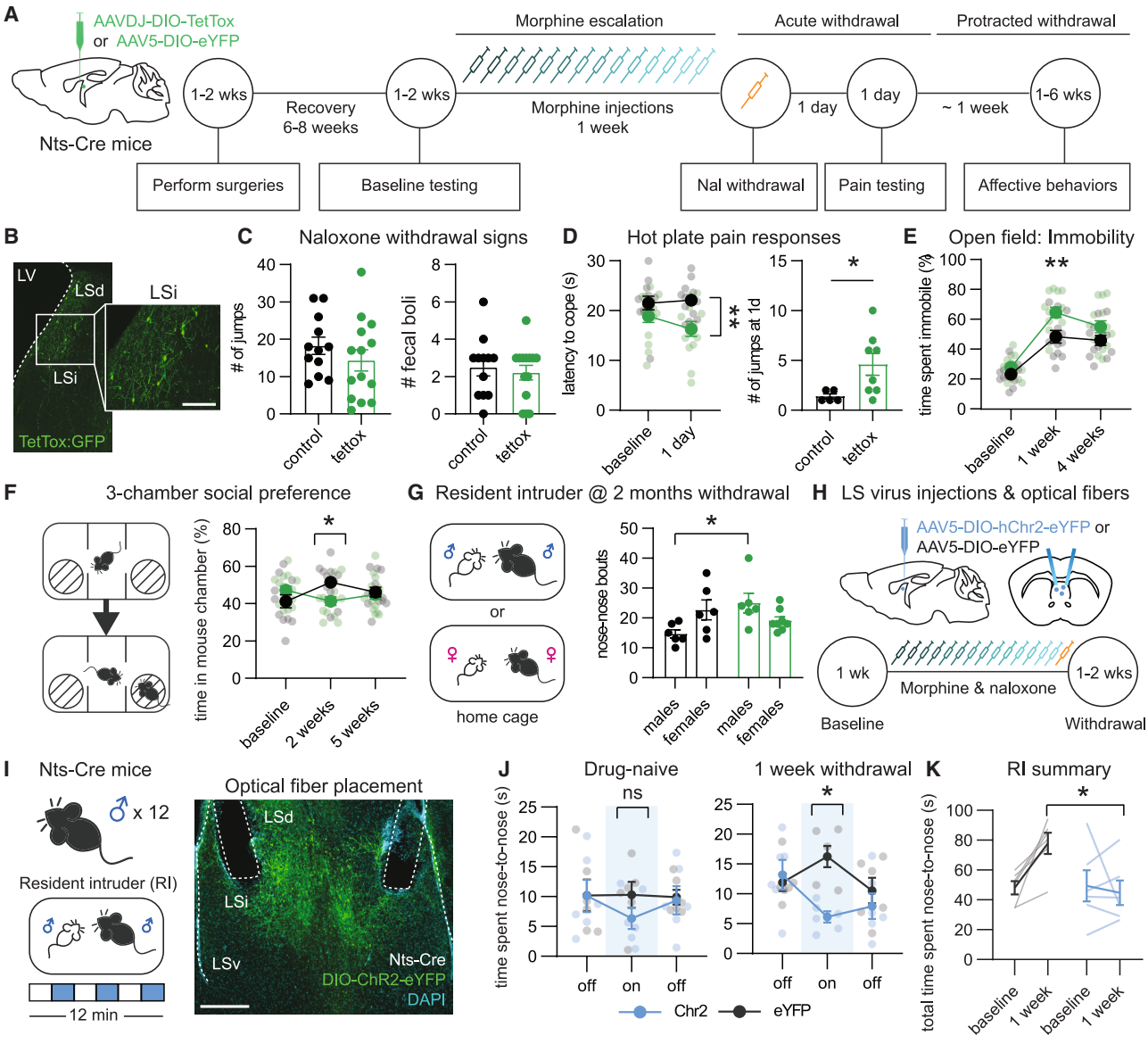

Figure 7. Silencing LS-*Nts* neurons exacerbates withdrawal-induced pain coping and triggers sexually dimorphic alterations in sociability

(A) Experimental schematic. *Nts*-Cre mice were bilaterally injected with AAV5-EF1a-DIO-eYFP or AAVDJ-EF1a-DIO-TetTox-GFP into the LS and subsequently underwent Mor escalation.

(B) Representative image of TetTox-GFP expression in the LSi. Scale bar, 200 μm.

(C) Nal-induced withdrawal signs. Left, number of jumps. Right, fecal boli.

(D) Hot plate. Left, latency to coping action (hind paw lick or jump). Right, TetTox increases the number of jumps mice perform at 1 day of withdrawal.

(E) Open field mobility.

(F) 3-chamber social preference.

(G) Left, RI assay. Right, nose-to-nose interactions.

(H) Experimental schematic. Male *Nts*-Cre mice were bilaterally injected with either AAV5-Ef1a-DIO-eYFP or AAV5-Ef1a-DIO-hChR2-eYFP, and bilateral optical fibers were implanted above the LS.

(I) Left, RI task, composed of 2-min-long light-off and light-on epochs. Right, representative optical fiber placement. Scale bar, 400 μm.

(J) Left, time spent interacting with an intruder mouse in the drug-naive context. Right, time spent interacting at 1 week of opioid withdrawal.

(K) Cumulative time of nose-to-nose interactions. All statistics are reported in Table S2. All data are represented as mean ± SEM. #$p < 0.1$, *$p < 0.05$, **$p < 0.01$, ***$p < 0.001$, ***$p < 0.001$, ****$p < 0.0001$.

Please cite this article in press as: Simon et al., Opioid-driven disruption of the septum reveals a role for neurotensin-expressing neurons in withdrawal, Neuron (2025), https://doi.org/10.1016/j.neuron.2025.04.024

based on context.[9,18,33,65,66] In fact, the LS may be organized as a lateral inhibition network, where extra-septal glutamatergic input drives different LS cell types to compete with one another.[17] This poses a system where certain LS neurons are preferentially recruited during stress and suppress the activity of other LS cell types to gate behavioral output.[7,17,18] The precise mechanisms through which LS cell types are recruited during opioid withdrawal are unclear. Although *Oprm1* was found to be globally expressed in the septum, its expression across cell clusters was not predictive of overall transcriptional perturbation during chronic Mor treatment. Our analyses instead suggested that the primary driver for LS opioid-induced DEGs may be inputs into the LS. Chronic Mor globally upregulated genes involved in postsynaptic neurotransmission, consistent with what has been reported in other brain areas.[41,67] Furthermore, cell-type-specific DEGs included genes encoding proteins that regulate excitability and synaptic transmission, which may reflect alterations in input-output connectivity. Indeed, opioid dependence perturbed several of our cell clusters, including LS-*Nts* (Gaba8), LS-*Sst* (Gaba11), LS-*Foxp2* (Gaba7), and glutamatergic neurons in the MS (Glu2)—which may together form an intra-septal network that facilitates the emergence of opioid-modulated behaviors. To our surprise, however, Nal-precipitated withdrawal robustly induced gene expression changes in primarily LS-*Nts* neurons (Figures 3C–3E). It is possible that Nal-induced LS-*Nts* activation rapidly suppresses the activity of adjacent septal neurons, such as LS-*Esr1*, which showed a transcriptional signature consistent with delayed activation following Nal treatment. Incidentally, LS-*Esr1* neurons may be important for methamphetamine-related phenotypes.[64]

The potential granularity of LS-*Nts* subtypes

Our snRNA-seq and HCR data indicated that *Nts* expression overlaps with *Sst*, *Foxp2*, *Drd3*, *Met*, and *Crhr2*, which are molecular markers that form layers within the septal complex. We found through *in situ Fos* analysis that cells co-expressing *Nts* and *Met* are modulated by Nal, and these cells were located in the central/caudal LSi. Though, interestingly, we detected a few cells that co-express *Nts* and *Met* in the snRNA-seq, but this is consistent with other sequencing studies detecting low or no levels of *Nts* in their data.[36] It is possible that the expression of *Nts*, or other genes, is underrepresented by snRNA-seq, somewhat limiting our ability to fully explore the granularity of LS-*Nts* subtypes or their intersection with other cell populations. The gradient-like cytoarchitecture of the septum poses opportunities for intersectional genetic tools to dissect the precise behavioral properties of each lamina, as a current standing question in the septal field is whether transcriptional profile or spatial domain is more predictive for the function of LS neurons.[17,37]

A persisting unknown in our present work concerns the major and minor inputs that selectively recruit LS-*Nts* neurons during opioid withdrawal. Historical literature and other contemporary work suggest that LS-*Nts* neurons likely receive inputs from the dorsal and ventral CA1 and dorsal and ventral CA3 regions of the hippocampus,[7,37,68] which is likely the largest source for glutamate in the septum. LS neurons occupying a similar spatial niche as LS-*Nts* neurons also receive fibers from the basolateral amygdala.[37] Smaller sources of subcortical glutamate may stem from the ventral tegmental area,[69] the LH,[70,71] and the paraventricular nucleus of the hypothalamus.[72] To assess potential input-specific regulation of LS-*Nts* neurons, we leveraged our data to identify potential subtypes that may be regulated by different inputs. IEG enrichment analysis of *Nts*+ cells expressing different receptor-encoding genes indicated that cells co-expressing *Nts* and *Drd2* or *Ntrk2* are more likely than other membrane receptor-expressing *Nts*+ cells to be activated following Nal-precipitated withdrawal. This is not surprising, given the well-documented role for dopamine in mediating both the rewarding and aversive effects of opioid use and withdrawal, respectively.[73,74] Investigating the precise dopamine signaling dynamics onto LS-*Nts* neurons and the general septal complex may shed light on additional mechanisms that perpetuate substance misuse. Moreover, *Ntrk2* encodes tropomyosin receptor kinase b (Trkb), and brain-derived neurotrophic factor (BDNF) signaling through Trkb has also been implicated in opioid-induced neuroplasticity,[75–77] opioid-mediated pain relief,[78] and in regulating LS-directed social behaviors,[36,79] so future work should more closely examine the role for neurotrophic signaling onto LS-*Nts* neurons in opioid-induced changes of pain expression and sociability.

The role for LS-*Nts* neurons in behavioral adaptation during opioid withdrawal

In this study, we show that opioid withdrawal elevates LS-*Nts* activity. Opioid withdrawal is arguably a chronic stress state,[1,3,22,80] and other states of chronic distress, such as pain and chronic social defeat, also elevate neuronal activity in the LS, including in LS-*Nts*, LS-*Sst*, and general LS GABAergic neurons.[34,61,81] Although Nal rapidly restored LS-*Nts* activity in opioid-dependent mice, these neurons did not appear necessary for mediating somatic signs of withdrawal. Instead, LS-*Nts* activity drives withdrawal-related behaviors that tend to emerge during protracted withdrawal. We originally hypothesized that prolonged LS-*Nts* activation would be maladaptive, but our results indicated the opposite. During opioid withdrawal, LS-*Nts* neurons promote analgesia, modulate risk-taking behaviors, and alter how mice approach unfamiliar conspecifics, which could have sex-specific consequences. In other words, LS-*Nts* hyperactivity may drive a series of behavioral responses that are adaptive when the animal is in a weakened, compromised, or uncertain state. Although chronic stress states may be driven by different stimuli (e.g., pain, emotional stress, or drug withdrawal), there is a convergent mechanism that drives LS activity upward in chronic stress settings. Our snRNA-seq data revealed that LS-*Nts* neurons are enriched for genes encoding receptors for neuromodulators, including *Drd2* and *Ntrk2*, which have both been extensively studied in the context of drug craving and relapse.[82,83] These observations form a rationale for studying how opioid withdrawal disrupts input regulation onto LS cell types and highlight the potential role for LS-*Nts* activity across multiple stress modalities.

Limitations of the study

Although we were able to leverage our snRNA-seq data to identify septal cell types putatively involved in withdrawal, our measures of "activation" were limited. Our snRNA-seq analyses

relied on a panel of IEGs rather than *Fos* alone, as our dataset did not possess many *Fos* transcripts. For our *in situ* experiments, we used the well-validated activity marker *Fos* to show that LS-*Nts* neurons are activated in opioid-withdrawn mice, but we did not examine other activity-regulated genes implicated in our snRNA-seq data, posing rationale for future work on cell-type-specific and input-specific IEG expression in the septum. Furthermore, we did not model protracted opioid withdrawal in our snRNA-seq experiment, limiting the conclusions we can draw regarding the neurophysiological changes that LS-*Nts* neurons undergo during acute and chronic opioid withdrawal. Studies on other key brain regions indicate that prolonged opioid withdrawal triggers widespread transcriptional alterations[84–87] that may be distinct from changes induced by Nal. Finally, we did not closely examine the precise neurocircuit and molecular mechanisms driving LS-*Nts* activity during opioid withdrawal. We focused primarily on LS-*Nts* neurons, but septal cell types are differentially impacted by chronic opioids and are likely to be interconnected with LS-*Nts* neurons.[17] *Oprm1* expression is also widely expressed throughout the LS, but it is unknown whether the mu opioid receptor is located pre- or post-synaptically in LS neurons, which would have different circuit-level implications for the involvement of the septum in withdrawal-induced behavioral changes. Indeed, the coordination of intra-septal connectivity, extra-septal inputs, and opioidergic signaling in driving LS-*Nts* activity and corresponding behavioral changes will pose an interesting avenue for future investigation—especially in the context of OUD.

The LS is a unique and heterogeneous limbic structure that performs a diverse role in motivated behaviors, but the precise LS cell types involved in opioid withdrawal were unknown. To address this, we generated the first functional atlas of the septum in opioid dependence and discovered that LS-*Nts* neurons are selectively recruited during opioid withdrawal. Using genetically targeted tools and a combination of *in situ*, *ex vivo*, and *in vivo* approaches, we present here the first demonstration of the multifaceted role for LS-*Nts* neurons in behavioral adaptation during opioid withdrawal. Given that LS-*Nts* neurons are involved in diverse behaviors, smaller subtypes may comprise the greater *Nts*+ population in the septum and perform distinct behavioral functions. LS-*Nts* neurons also project to diverse brain areas, as shown here and in other studies,[7,68,88] which may be reflected in their molecular diversity. Together, our results emphasize the LS as a key region disrupted by opioid dependence and implicate a new potential therapeutic target in persons with OUD, and our snRNA-seq data will provide a comprehensive resource for opioid-perturbed transcriptional alterations in the septum, revealing ample opportunity for future targeted studies on molecularly defined septal neurons.

RESOURCE AVAILABILITY

Lead contact

Further information and requests for resources and reagents should be directed to and will be fulfilled by Garret Stuber (gstuber@uw.edu).

Materials availability

This study did not generate new, unique reagents or strains.

Data and code availability

The NCBI Gene Expression Omnibus accession number associated with this study's raw snRNA-seq data is GSE236007. All the code used to analyze scRNA-seq, HCR, and two-photon imaging data are available at a GitHub repository affiliated with the Stuber Laboratory group and this manuscript (https://doi.org/10.5281/zenodo.15226356). Finally, filtered and processed snRNA-seq and HCR files are available on Zenodo (https://doi.org/10.5281/zenodo.15006781). Any additional information required to reanalyze the data reported in this paper is available from the lead contact upon request.

ACKNOWLEDGMENTS

We thank the lab of Richard D. Palmiter for the *Sst*-Cre mice and TetTox virus and the lab of Larry S. Zweifel for the *Nts*-Cre line. This work was supported by the University of Washington Addictions, Drug & Alcohol Institute (UW ADAI) (R.C.S.) and NIH grants R01 DA054317, R01 DA059388, R37 DA032750, R01 DA038168 (G.D.S.), R01DA059374 (S.A.G.), and F31 MH117931 (R.C.S.). This work was also supported by the University of Washington Center of Excellence in Neurobiology of Addiction, Pain, and Emotion (NAPE Center, P30 DA048736).

AUTHOR CONTRIBUTIONS

Conceptualization, R.C.S. and G.D.S.; methodology, R.C.S. and G.D.S.; validation, R.C.S. and B.A.B.; formal analysis, R.C.S., W.T.F., B.A.B., P.S., K.K.I., and K.H.; investigation, R.C.S., W.T.F., B.A.B., M.T., K.K.I., M.M.H., M.M.M., and A.D.S.; resources, G.D.S. and S.A.G.; data curation, R.C.S. and P.S.; writing – original draft, R.C.S. and G.D.S.; writing – review and editing, R.C.S. and G.D.S. with input from all authors; visualization, R.C.S., P.S., W.T.F., and K.I.; supervision, G.D.S.; and funding acquisition, G.D.S. and R.C.S.

DECLARATION OF INTERESTS

The authors declare no competing interests.

STAR★METHODS

Detailed methods are provided in the online version of this paper and include the following:

- Sample integration and clustering
- DEG analysis
- IEG analysis
- Classifier analysis
- HCR analysis
- Correlation between snRNAseq and HCR
- Calculating naloxone-induced IEG expression changes
- Calculating acute morphine or naloxone-induced IEG expression changes
- Two-photon analysis
- Spontaneous activity analysis
- Evoked activity analysis

SUPPLEMENTAL INFORMATION

Supplemental information can be found online at https://doi.org/10.1016/j.neuron.2025.04.024.

Received: March 14, 2024
Revised: March 14, 2025
Accepted: April 25, 2025
Published: May 15, 2025

REFERENCES

1. Koob, G.F., and Le Moal, M. (2001). Drug Addiction, Dysregulation of Reward, and Allostasis. Neuropsychopharmacology *24*, 97–129. https://doi.org/10.1016/S0893-133X(00)00195-0.
2. George, O., and Koob, G.F. (2017). Individual differences in the neuropsychopathology of addiction. Dial. Clin. Neurosci. *19*, 217–229. https://doi.org/10.31887/DCNS.2017.19.3/gkoob.
3. Welsch, L., Bailly, J., Darcq, E., and Kieffer, B.L. (2020). The Negative Affect of Protracted Opioid Abstinence: Progress and Perspectives From Rodent Models. Biol. Psychiatry *87*, 54–63. https://doi.org/10.1016/j.biopsych.2019.07.027.
4. Olds, J., and Milner, P. (1954). Positive reinforcement produced by electrical stimulation of septal area and other regions of rat brain. J. Comp. Physiol. Psychol. *47*, 419–427. https://doi.org/10.1037/h0058775.
5. Wong, L.C., Wang, L., D'Amour, J.A., Yumita, T., Chen, G., Yamaguchi, T., Chang, B.C., Bernstein, H., You, X., Feng, J.E., et al. (2016). Effective Modulation of Male Aggression through Lateral Septum to Medial Hypothalamus Projection. Curr. Biol. *26*, 593–604. https://doi.org/10.1016/j.cub.2015.12.065.
6. Brady, J.V., and Nauta, W.J. (1953). Subcortical mechanisms in emotional behavior: affective changes following septal forebrain lesions in the albino rat. J. Comp. Physiol. Psychol. *46*, 339–346. https://doi.org/10.1037/h0059531.
7. Sheehan, T.P., Chambers, R.A., and Russell, D.S. (2004). Regulation of affect by the lateral septum: implications for neuropsychiatry. Brain Res. Brain Res. Rev. *46*, 71–117. https://doi.org/10.1016/j.brainresrev.2004.04.009.
8. Luo, A.H., Tahsili-Fahadan, P., Wise, R.A., Lupica, C.R., and Aston-Jones, G. (2011). Linking Context with Reward: A Functional Circuit from Hippocampal CA3 to Ventral Tegmental Area. Science *333*, 353–357. https://doi.org/10.1126/science.1204622.
9. McGlinchey, E.M., and Aston-Jones, G. (2018). Dorsal Hippocampus Drives Context-Induced Cocaine Seeking via Inputs to Lateral Septum. Neuropsychopharmacology *43*, 987–1000. https://doi.org/10.1038/npp.2017.144.
10. Kozell, L.B., Hitzemann, R., and Buck, K.J. (2005). Acute Alcohol Withdrawal is Associated with c-Fos Expression in the Basal Ganglia and Associated Circuitry: C57BL/6J and DBA/2J Inbred Mouse Strain Analyses. Alcohol. Clin. Exp. Res. *29*, 1939–1948. https://doi.org/10.1097/01.alc.0000187592.57853.12.
11. Haun, H.L., D'Ambrosio, S.L., Pati, D., Taxier, L.R., and Kash, T.L. (2022). Activation of the dorsal septum increases alcohol consumption in male C57BL/6J mice. Addict. Neurosci. *3*, 100023. https://doi.org/10.1016/j.addicn.2022.100023.
12. Franklin, T.R., and Druhan, J.P. (2000). Expression of Fos-related antigens in the nucleus accumbens and associated regions following exposure to a cocaine-paired environment. Eur. J. Neurosci. *12*, 2097–2106. https://doi.org/10.1046/j.1460-9568.2000.00071.x.
13. Pantazis, C.B., and Aston-Jones, G. (2020). Lateral septum inhibition reduces motivation for cocaine: Reversal by diazepam. Addict. Biol. *25*, e12742. https://doi.org/10.1111/adb.12742.
14. Le Merrer, J., Gavello-Baudy, S., Galey, D., and Cazala, P. (2007). Morphine self-administration into the lateral septum depends on dopaminergic mechanisms: Evidence from pharmacology and Fos neuroimaging. Behav. Brain Res. *180*, 203–217. https://doi.org/10.1016/j.bbr.2007.03.014.
15. Li, Y.-L., Wei, S., Liu, Q., Gong, Q., Zhang, Q.-J., Zheng, T.-G., Yong, Z., Chen, F., Lawrence, A.J., and Liang, J.-H. (2022). Mu-opioid receptors in septum mediate the development of behavioural sensitization to a single morphine exposure in male rats. Addict. Biol. *27*, e13066. https://doi.org/10.1111/adb.13066.
16. Valentino, R.J., and Volkow, N.D. (2018). Untangling the complexity of opioid receptor function. Neuropsychopharmacology *43*, 2514–2520. https://doi.org/10.1038/s41386-018-0225-3.
17. Besnard, A., and Leroy, F. (2022). Top-down regulation of motivated behaviors via lateral septum sub-circuits. Mol. Psychiatry *27*, 3119–3128. https://doi.org/10.1038/s41380-022-01599-3.
18. Rizzi-Wise, C.A., and Wang, D.V. (2021). Putting Together Pieces of the Lateral Septum: Multifaceted Functions and Its Neural Pathways. eNeuro *8*, ENEURO.0315-21.2021. https://doi.org/10.1523/ENEURO.0315-21.2021.
19. Anthony, T.E., Dee, N., Bernard, A., Lerchner, W., Heintz, N., and Anderson, D.J. (2014). Control of Stress-Induced Persistent Anxiety by an Extra-Amygdala Septohypothalamic Circuit. Cell *156*, 522–536. https://doi.org/10.1016/j.cell.2013.12.040.
20. Shin, S., Pribiag, H., Lilascharoen, V., Knowland, D., Wang, X.-Y., and Lim, B.K. (2018). Drd3 Signaling in the Lateral Septum Mediates Early Life Stress-Induced Social Dysfunction. Neuron *97*, 195–208.e6. https://doi.org/10.1016/j.neuron.2017.11.040.
21. Azevedo, E.P., Tan, B., Pomeranz, L.E., Ivan, V., Fetcho, R., Schneeberger, M., Doerig, K.R., Liston, C., Friedman, J.M., and Stern, S.A. (2020). A limbic circuit selectively links active escape to food suppression. eLife *9*, e58894. https://doi.org/10.7554/eLife.58894.
22. Koob, G.F. (2020). Neurobiology of Opioid Addiction: Opponent Process, Hyperkatifeia, and Negative Reinforcement. Biol. Psychiatry *87*, 44–53. https://doi.org/10.1016/j.biopsych.2019.05.023.
23. DePasquale, E.A.K., Schnell, D.J., Van Camp, P.-J., Valiente-Alandí, Í., Blaxall, B.C., Grimes, H.L., Singh, H., and Salomonis, N. (2019). DoubletDecon: Deconvoluting Doublets from Single-Cell RNA-Sequencing Data. Cell Rep. *29*, 1718–1727.e8. https://doi.org/10.1016/j.celrep.2019.09.082.
24. Butler, A., Hoffman, P., Smibert, P., Papalexi, E., and Satija, R. (2018). Integrating single-cell transcriptomic data across different conditions, technologies, and species. Nat. Biotechnol. *36*, 411–420. https://doi.org/10.1038/nbt.4096.
25. Haghverdi, L., Lun, A.T.L., Morgan, M.D., and Marioni, J.C. (2018). Batch effects in single-cell RNA-sequencing data are corrected by matching mutual nearest neighbors. Nat. Biotechnol. *36*, 421–427. https://doi.org/10.1038/nbt.4091.
26. Macosko, E.Z., Basu, A., Satija, R., Nemesh, J., Shekhar, K., Goldman, M., Tirosh, I., Bialas, A.R., Kamitaki, N., Martersteck, E.M., et al. (2015). Highly Parallel Genome-wide Expression Profiling of Individual Cells

Using Nanoliter Droplets. Cell *161*, 1202–1214. https://doi.org/10.1016/j.cell.2015.05.002.

27. Wu, Y.E., Pan, L., Zuo, Y., Li, X., and Hong, W. (2017). Detecting Activated Cell Populations Using Single-Cell RNA-Seq. Neuron *96*, 313–329.e6. https://doi.org/10.1016/j.neuron.2017.09.026.
28. Zeisel, A., Hochgerner, H., Lönnerberg, P., Johnsson, A., Memic, F., van der Zwan, J., Häring, M., Braun, E., Borm, L.E., La Manno, G., et al. (2018). Molecular Architecture of the Mouse Nervous System. Cell *174*, 999–1014.e22. https://doi.org/10.1016/j.cell.2018.06.021.
29. Rossi, M.A., Basiri, M.L., McHenry, J.A., Kosyk, O., Otis, J.M., van den Munkhof, H.E., Bryois, J., Hübel, C., Breen, G., Guo, W., et al. (2019). Obesity remodels activity and transcriptional state of a lateral hypothalamic brake on feeding. Science *364*, 1271–1274. https://doi.org/10.1126/science.aax1184.
30. Hashikawa, Y., Hashikawa, K., Rossi, M.A., Basiri, M.L., Liu, Y., Johnston, N.L., Ahmad, O.R., and Stuber, G.D. (2020). Transcriptional and Spatial Resolution of Cell Types in the Mammalian Habenula. Neuron *106*, 743–758.e5. https://doi.org/10.1016/j.neuron.2020.03.011.
31. Rossi, M.A., Basiri, M.L., Liu, Y., Hashikawa, Y., Hashikawa, K., Fenno, L.E., Kim, Y.S., Ramakrishnan, C., Deisseroth, K., and Stuber, G.D. (2021). Transcriptional and functional divergence in lateral hypothalamic glutamate neurons projecting to the lateral habenula and ventral tegmental area. Neuron *109*, 3823–3837.e6. https://doi.org/10.1016/j.neuron.2021.09.020.
32. Chen, Z., Chen, G., Zhong, J., Jiang, S., Lai, S., Xu, H., Deng, X., Li, F., Lu, S., Zhou, K., et al. (2022). A circuit from lateral septum neurotensin neurons to tuberal nucleus controls hedonic feeding. Mol. Psychiatry *27*, 4843–4860. https://doi.org/10.1038/s41380-022-01742-0.
33. Besnard, A., Gao, Y., TaeWoo Kim, M., Twarkowski, H., Reed, A.K., Langberg, T., Feng, W., Xu, X., Saur, D., Zweifel, L.S., et al. (2019). Dorsolateral septum somatostatin interneurons gate mobility to calibrate context-specific behavioral fear responses. Nat. Neurosci. *22*, 436–446. https://doi.org/10.1038/s41593-018-0330-y.
34. Li, H., Sung, H.H., and Lau, C.G. (2022). Activation of Somatostatin-Expressing Neurons in the Lateral Septum Improves Stress-Induced Depressive-like Behaviors in Mice. Pharmaceutics *14*, 2253. https://doi.org/10.3390/pharmaceutics14102253.
35. Hashimoto, M., Brito, S.I., Venner, A., Pasqualini, A.L., Yang, T.L., Allen, D., Fuller, P.M., and Anthony, T.E. (2022). Lateral septum modulates cortical state to tune responsivity to threat stimuli. Cell Rep. *41*, 111521. https://doi.org/10.1016/j.celrep.2022.111521.
36. Rodriguez, L.A., Tran, M.N., Garcia-Flores, R., Oh, S., Phillips, R.A., Pattie, E.A., Divecha, H.R., Kim, S.H., Shin, J.H., Lee, Y.K., et al. (2024). TrkB-dependent regulation of molecular signaling across septal cell types. Transl. Psychiatry *14*, 52. https://doi.org/10.1038/s41398-024-02758-6.
37. Reid, C.M., Ren, Y., Xie, Y., García, M.T., Tran, D., Vu, S., Liu, J., Adam, M.A., Hanson, S.M., Pisco, A.O., et al. (2024). Multimodal classification of neurons in the lateral septum. Preprint at bioRxiv. https://doi.org/10.1101/2024.02.15.580381.
38. Yao, Z., van Velthoven, C.T.J., Kunst, M., Zhang, M., McMillen, D., Lee, C., Jung, W., Goldy, J., Abdelhak, A., Baker, P., et al. (2023). A high-resolution transcriptomic and spatial atlas of cell types in the whole mouse brain. Preprint at bioRxiv. https://doi.org/10.1101/2023.03.06.531121.
39. McClung, C.A., Nestler, E.J., and Zachariou, V. (2005). Regulation of Gene Expression by Chronic Morphine and Morphine Withdrawal in the Locus Ceruleus and Ventral Tegmental Area. J. Neurosci. *25*, 6005–6015. https://doi.org/10.1523/JNEUROSCI.0062-05.2005.
40. Shaw-Lutchman, T.Z., Barrot, M., Wallace, T., Gilden, L., Zachariou, V., Impey, S., Duman, R.S., Storm, D., and Nestler, E.J. (2002). Regional and Cellular Mapping of cAMP Response Element-Mediated Transcription during Naltrexone-Precipitated Morphine Withdrawal. J. Neurosci. *22*, 3663–3672. https://doi.org/10.1523/JNEUROSCI.22-09-03663.2002.
41. Mazei-Robison, M.S., and Nestler, E.J. (2012). Opiate-Induced Molecular and Cellular Plasticity of Ventral Tegmental Area and Locus Coeruleus Catecholamine Neurons. Cold Spring Harb. Perspect. Med. *2*, a012070. https://doi.org/10.1101/cshperspect.a012070.
42. West, A.E., and Greenberg, M.E. (2011). Neuronal Activity-Regulated Gene Transcription in Synapse Development and Cognitive Function. Cold Spring Harb. Perspect. Biol. *3*, a005744. https://doi.org/10.1101/cshperspect.a005744.
43. Kovács, K.J. (2008). Measurement of Immediate-Early Gene Activation-c-fos and Beyond. J. Neuroendocrinol. *20*, 665–672. https://doi.org/10.1111/j.1365-2826.2008.01734.x.
44. Bullitt, E. (1990). Expression ofC-fos-like protein as a marker for neuronal activity following noxious stimulation in the rat. J. Comp. Neurol. *296*, 517–530. https://doi.org/10.1002/cne.902960402.
45. Skinnider, M.A., Squair, J.W., Kathe, C., Anderson, M.A., Gautier, M., Matson, K.J.E., Milano, M., Hutson, T.H., Barraud, Q., Phillips, A.A., et al. (2021). Cell type prioritization in single-cell data. Nat. Biotechnol. *39*, 30–34. https://doi.org/10.1038/s41587-020-0605-1.
46. Kong, H., Raynor, K., Yano, H., Takeda, J., Bell, G.I., and Reisine, T. (1994). Agonists and antagonists bind to different domains of the cloned c opioid receptor. Proc. Natl. Acad. Sci. USA *91*, 8042–8046.
47. von Buchholtz, L.J., Ghitani, N., Lam, R.M., Licholai, J.A., Chesler, A.T., and Ryba, N.J.P. (2021). Decoding Cellular Mechanisms for Mechanosensory Discrimination. Neuron *109*, 285–298.e5. https://doi.org/10.1016/j.neuron.2020.10.028.
48. Choi, H.M.T., Schwarzkopf, M., Fornace, M.E., Acharya, A., Artavanis, G., Stegmaier, J., Cunha, A., and Pierce, N.A. (2018). Third-generation *in situ* hybridization chain reaction: multiplexed, quantitative, sensitive, versatile, robust. Development *145*, dev165753. https://doi.org/10.1242/dev.165753.
49. Turrero García, M., Stegmann, S.K., Lacey, T.E., Reid, C.M., Hrvatin, S., Weinreb, C., Adam, M.A., Nagy, M.A., and Harwell, C.C. (2021). Transcriptional profiling of sequentially generated septal neuron fates. eLife *10*, e71545. https://doi.org/10.7554/eLife.71545.
50. Dragunow, M., and Faull, R. (1989). The use of c-fos as a metabolic marker in neuronal pathway tracing. J. Neurosci. Methods *29*, 261–265. https://doi.org/10.1016/0165-0270(89)90150-7.
51. Kiluk, B.D., Yip, S.W., DeVito, E.E., Carroll, K.M., and Sofuoglu, M. (2019). Anhedonia as a Key Clinical Feature in the Maintenance and Treatment of Opioid Use Disorder. Clin. Psychol. Sci. *7*, 1190–1206. https://doi.org/10.1177/2167702619855659.
52. Carcoba, L.M., Contreras, A.E., Cepeda-Benito, A., and Meagher, M.W. (2011). Negative Affect Heightens Opiate Withdrawal-Induced Hyperalgesia in Heroin Dependent Individuals. J. Addict. Dis. *30*, 258–270. https://doi.org/10.1080/10550887.2011.581985.
53. Pellizzari, R., Rossetto, O., Schiavo, G., and Montecucco, C. (1999). Tetanus and botulinum neurotoxins: mechanism of action and therapeutic uses. Philos. Trans. R. Soc. Lond. B Biol. Sci. *354*, 259–268. https://doi.org/10.1098/rstb.1999.0377.
54. Bravo, I.M., Luster, B.R., Flanigan, M.E., Perez, P.J., Cogan, E.S., Schmidt, K.T., and McElligott, Z.A. (2020). Divergent behavioral responses in protracted opioid withdrawal in male and female C57BL/6J mice. Eur. J. Neurosci. *51*, 742–754. https://doi.org/10.1111/ejn.14580.
55. Matthes, H.W.D., Maldonadot, R., Simonin, F., Valverdet, O., and Slowet, S. (1996). Loss of Morphine-Induced Analgesia, Reward Effect and Withdrawal Symptoms in Mice Lacking the f.l·Opioid-receptor gene. Nature *383*, 819–823.
56. Alvarez-Bagnarol, Y., Marchette, R.C.N., Francis, C., Morales, M.M., and Vendruscolo, L.F. (2022). Neuronal Correlates of Hyperalgesia and Somatic Signs of Heroin Withdrawal in Male and Female Mice. eNeuro *9*, ENEURO.0106-22.2022. https://doi.org/10.1523/ENEURO.0106-22.2022.

57. Babor, T.F., Meyer, R.E., Mirin, S.M., McNamee, H.B., and Davies, M. (1976). Behavioral and Social Effects of Heroin Self-Administration and Withdrawal. Arch. Gen. Psychiatry *33*, 363–367. https://doi.org/10.1001/archpsyc.1976.01770030067010.

58. Piccin, A., and Contarino, A. (2022). The CRF $_1$ receptor mediates social behavior deficits induced by opiate withdrawal. J. Neurosci. Res. *100*, 309–321. https://doi.org/10.1002/jnr.24697.

59. Young, K.A., Gobrogge, K.L., and Wang, Z. (2011). The role of mesocorticolimbic dopamine in regulating interactions between drugs of abuse and social behavior. Neurosci. Biobehav. Rev. *35*, 498–515. https://doi.org/10.1016/j.neubiorev.2010.06.004.

60. Menon, R., Süß, T., Oliveira, V.E. de M., Neumann, I.D., and Bludau, A. (2022). Neurobiology of the lateral septum: regulation of social behavior. Trends Neurosci. *45*, 27–40. https://doi.org/10.1016/j.tins.2021.10.010.

61. Li, L., Durand-de Cuttoli, R., Aubry, A.V., Burnett, C.J., Cathomas, F., Parise, L.F., Chan, K.L., Morel, C., Yuan, C., Shimo, Y., et al. (2023). Social trauma engages lateral septum circuitry to occlude social reward. Nature *613*, 696–703. https://doi.org/10.1038/s41586-022-05484-5.

62. Robison, A.J., and Nestler, E.J. (2011). Transcriptional and epigenetic mechanisms of addiction. Nat. Rev. Neurosci. *12*, 623–637. https://doi.org/10.1038/nrn3111.

63. Nestler, E.J., and Lüscher, C. (2019). The Molecular Basis of Drug Addiction: Linking Epigenetic to Synaptic and Circuit Mechanisms. Neuron *102*, 48–59. https://doi.org/10.1016/j.neuron.2019.01.016.

64. Chen, G., Lai, S., Jiang, S., Li, F., Sun, K., Wu, X., Zhou, K., Liu, Y., Deng, X., Chen, Z., et al. (2024). Cellular and circuit architecture of the lateral septum for reward processing. Neuron *112*, 2783–2798.e9. https://doi.org/10.1016/j.neuron.2024.06.004.

65. Décarie-Spain, L., Liu, C.M., Lauer, L.T., Subramanian, K., Bashaw, A.G., Klug, M.E., Gianatiempo, I.H., Suarez, A.N., Noble, E.E., Donohue, K.N., et al. (2022). Ventral hippocampus-lateral septum circuitry promotes foraging-related memory. Cell Rep. *40*, 111402. https://doi.org/10.1016/j.celrep.2022.111402.

66. Wirtshafter, H.S., and Wilson, M.A. (2020). Differences in reward biased spatial representations in the lateral septum and hippocampus. eLife *9*, e55252. https://doi.org/10.7554/eLife.55252.

67. Seney, M.L., Kim, S.-M., Glausier, J.R., Hildebrand, M.A., Xue, X., Zong, W., Wang, J., Shelton, M.A., Phan, B.N., Srinivasan, C., et al. (2021). Transcriptional Alterations in Dorsolateral Prefrontal Cortex and Nucleus Accumbens Implicate Neuroinflammation and Synaptic Remodeling in Opioid Use Disorder. Biol. Psychiatry *90*, 550–562. https://doi.org/10.1016/j.biopsych.2021.06.007.

68. Risold, P.Y., and Swanson, L.W. (1997). Connections of the rat lateral septal complex. Brain Res. Brain Res. Rev. *24*, 115–195. https://doi.org/10.1016/S0165-0173(97)00009-X.

69. Leroy, F., Park, J., Asok, A., Brann, D.H., Meira, T., Boyle, L.M., Buss, E.W., Kandel, E.R., and Siegelbaum, S.A. (2018). A circuit from hippocampal CA2 to lateral septum disinhibits social aggression. Nature *564*, 213–218. https://doi.org/10.1038/s41586-018-0772-0.

70. Lewis, K., Li, C., Perrin, M.H., Blount, A., Kunitake, K., Donaldson, C., Vaughan, J., Reyes, T.M., Gulyas, J., Fischer, W., et al. (2001). Identification of urocortin III, an additional member of the corticotropin-releasing factor (CRF) family with high affinity for the CRF2 receptor. Proc. Natl. Acad. Sci. USA *98*, 7570–7575. https://doi.org/10.1073/pnas.121165198.

71. Horii-Hayashi, N., Nomoto, K., Endo, N., Yamanaka, A., Kikusui, T., and Nishi, M. (2021). Hypothalamic perifornical Urocortin-3 neurons modulate defensive responses to a potential threat stimulus. iScience *24*, 101908. https://doi.org/10.1016/j.isci.2020.101908.

72. Li, Y.-C., Wang, Q., Li, M.-G., Hu, S.-F., and Xu, G.-Y. (2023). A paraventricular hypothalamic nucleus input to ventral of lateral septal nucleus controls chronic visceral pain. Pain *164*, 625–637. https://doi.org/10.1097/j.pain.0000000000002750.

73. Doyle, M.A., and Mazei-Robison, M.S. (2021). Opioid-Induced Molecular and Cellular Plasticity of Ventral Tegmental Area Dopamine Neurons. Cold Spring Harb. Perspect. Med. *11*, a039362. https://doi.org/10.1101/cshperspect.a039362.

74. Langlois, L.D., and Nugent, F.S. (2017). Opiates and Plasticity in the Ventral Tegmental Area. ACS Chem. Neurosci. *8*, 1830–1838. https://doi.org/10.1021/acschemneuro.7b00281.

75. Vargas-Perez, H., Bahi, A., Bufalino, M.R., Ting-a-Kee, R., Maal-Bared, G., Lam, J., Fahmy, A., Clarke, L., Blanchard, J.K., Larsen, B.R., et al. (2014). BDNF Signaling in the VTA Links the Drug-Dependent State to Drug Withdrawal Aversions. J. Neurosci. *34*, 7899–7909. https://doi.org/10.1523/JNEUROSCI.3776-13.2014.

76. Lloret-Torres, M.E., Ayala-Pagán, R.N., Martínez-Rivera, F.J., Bonilla-Rullán, P., and Barreto-Estrada, J.L. (2022). Hippocampal and amygdalar increased BDNF expression in the extinction of opioid-induced place preference. IBRO Neurosci. Rep. *13*, 402–409. https://doi.org/10.1016/j.ibneur.2022.10.007.

77. Akbarian, S., Rios, M., Liu, R.-J., Gold, S.J., Fong, H.-F., Zeiler, S., Coppola, V., Tessarollo, L., Jones, K.R., Nestler, E.J., et al. (2002). Brain-Derived Neurotrophic Factor Is Essential for Opiate-Induced Plasticity of Noradrenergic Neurons. J. Neurosci. *22*, 4153–4162. https://doi.org/10.1523/JNEUROSCI.22-10-04153.2002.

78. Lim, S.Y., and Cengiz, P. (2022). Opioid tolerance and opioid-induced hyperalgesia: Is TrkB modulation a potential pharmacological solution? Neuropharmacology *220*, 109260. https://doi.org/10.1016/j.neuropharm.2022.109260.

79. Rodriguez, L.A., Kim, S.-H., Page, S.C., Nguyen, C.V., Pattie, E.A., Hallock, H.L., Valerino, J., Maynard, K.R., Jaffe, A.E., and Martinowich, K. (2023). The basolateral amygdala to lateral septum circuit is critical for regulating social novelty in mice. Neuropsychopharmacology *48*, 529–539. https://doi.org/10.1038/s41386-022-01487-y.

80. Koob, G.F., and Volkow, N.D. (2016). Neurobiology of addiction: a neurocircuitry analysis. Lancet Psychiatry *3*, 760–773. https://doi.org/10.1016/S2215-0366(16)00104-8.

81. Wang, D., Pan, X., Zhou, Y., Wu, Z., Ren, K., Liu, H., Huang, C., Yu, Y., He, T., Zhang, X., et al. (2023). Lateral septum-lateral hypothalamus circuit dysfunction in comorbid pain and anxiety. Mol. Psychiatry *28*, 1090–1100. https://doi.org/10.1038/s41380-022-01922-y.

82. Volkow, N.D., Wise, R.A., and Baler, R. (2017). The dopamine motive system: implications for drug and food addiction. Nat. Rev. Neurosci. *18*, 741–752. https://doi.org/10.1038/nrn.2017.130.

83. Weinshenker, D., and Schroeder, J.P. (2007). There and Back Again: A Tale of Norepinephrine and Drug Addiction. Neuropsychopharmacology *32*, 1433–1451. https://doi.org/10.1038/sj.npp.1301263.

84. Wei, J., Lambert, T.Y., Valada, A., Patel, N., Walker, K., Lenders, J., Schmidt, C.J., Iskhakova, M., Alazizi, A., Mair-Meijers, H., et al. (2023). Single nucleus transcriptomics of ventral midbrain identifies glial activation associated with chronic opioid use disorder. Nat. Commun. *14*, 5610. https://doi.org/10.1038/s41467-023-41455-8.

85. Yan, Y., Truitt, B., Tao, J., Boyles, S.M., Antoine, D., Hulme, W., and Roy, S. (2023). Single-cell profiling of glial cells from the mouse amygdala under opioid dependent and withdrawal states. iScience *26*, 108166. https://doi.org/10.1016/j.isci.2023.108166.

86. O'Sullivan, S.J., Malahias, E., Park, J., Srivastava, A., Reyes, B.A.S., Gorky, J., Vadigepalli, R., Van Bockstaele, E.J., and Schwaber, J.S. (2019). Single-Cell Glia and Neuron Gene Expression in the Central Amygdala in Opioid Withdrawal Suggests Inflammation With Correlated Gut Dysbiosis. Front. Neurosci. *13*, 665. https://doi.org/10.3389/fnins.2019.00665.

87. Karagiannis, T.T., Cleary, J.P., Gok, B., Henderson, A.J., Martin, N.G., Yajima, M., Nelson, E.C., and Cheng, C.S. (2020). Single cell transcriptomics reveals opioid usage evokes widespread suppression of antiviral gene program. Nat. Commun. *11*, 2611. https://doi.org/10.1038/s41467-020-16159-y.

88. Risold, P.Y., and Swanson, L.W. (1997). Chemoarchitecture of the rat lateral septal nucleus1Published. Brain Res. Brain Res. Rev. *24*, 91–113. https://doi.org/10.1016/S0165-0173(97)00008-8.

89. Mendelev, N., Zamojski, M., Amper, M.A.S., Cheng, W.S., Pincas, H., Nair, V.D., Zaslavsky, E., Sealfon, S.C., and Ruf-Zamojski, F. (2022). Multi-omics profiling of single nuclei from frozen archived postmortem human pituitary tissue. Star Protoc. *3*, 101446. https://doi.org/10.1016/j.xpro.2022.101446.

90. Thrupp, N., Sala Frigerio, C., Wolfs, L., Skene, N.G., Fattorelli, N., Poovathingal, S., Fourne, Y., Matthews, P.M., Theys, T., Mancuso, R., et al. (2020). Single-Nucleus RNA-Seq Is Not Suitable for Detection of Microglial Activation Genes in Humans. Cell Rep. *32*, 108189. https://doi.org/10.1016/j.celrep.2020.108189.

91. Namboodiri, V.M.K., Otis, J.M., Van Heeswijk, K., Voets, E.S., Alghorazi, R.A., Rodriguez-Romaguera, J., Mihalas, S., and Stuber, G.D. (2019). Single-cell activity tracking reveals that orbitofrontal neurons acquire and maintain a long-term memory to guide behavioral adaptation. Nat. Neurosci. *22*, 1110–1121. https://doi.org/10.1038/s41593-019-0408-1.

92. Friard, O., and Gamba, M. (2016). BORIS: a free, versatile open-source event-logging software for video/audio coding and live observations. Methods Ecol. Evol. *7*, 1325–1330. https://doi.org/10.1111/2041-210X.12584.

93. Stuart, T., Butler, A., Hoffman, P., Hafemeister, C., Papalexi, E., Mauck, W.M., Hao, Y., Stoeckius, M., Smibert, P., and Satija, R. (2019). Comprehensive Integration of Single-Cell Data. Cell *177*, 1888–1902. e21. https://doi.org/10.1016/j.cell.2019.05.031.

94. Hafemeister, C., and Satija, R. (2019). Normalization and variance stabilization of single-cell RNA-seq data using regularized negative binomial regression. Genome Biol. *20*, 296. https://doi.org/10.1186/s13059-019-1874-1.

95. Zappia, L., and Oshlack, A. (2018). Clustering trees: a visualization for evaluating clusterings at multiple resolutions. GigaScience *7*, giy083. https://doi.org/10.1093/gigascience/giy083.

96. Kuleshov, M.V., Jones, M.R., Rouillard, A.D., Fernandez, N.F., Duan, Q., Wang, Z., Koplev, S., Jenkins, S.L., Jagodnik, K.M., Lachmann, A., et al. (2016). Enrichr: a comprehensive gene set enrichment analysis web server 2016 update. Nucleic Acids Res. *44*, W90–W97. https://doi.org/10.1093/nar/gkw377.

97. Chen, E.Y., Tan, C.M., Kou, Y., Duan, Q., Wang, Z., Meirelles, G.V., Clark, N.R., and Ma'ayan, A. (2013). Enrichr: interactive and collaborative HTML5 gene list enrichment analysis tool. BMC Bioinformatics *14*, 128. https://doi.org/10.1186/1471-2105-14-128.

98. Xie, Z., Bailey, A., Kuleshov, M.V., Clarke, D.J.B., Evangelista, J.E., Jenkins, S.L., Lachmann, A., Wojciechowicz, M.L., Kropiwnicki, E., Jagodnik, K.M., et al. (2021). Gene Set Knowledge Discovery with Enrichr. Curr. Protoc. *1*, e90. https://doi.org/10.1002/cpz1.90.

99. Bankhead, P., Loughrey, M.B., Fernández, J.A., Dombrowski, Y., McArt, D.G., Dunne, P.D., McQuaid, S., Gray, R.T., Murray, L.J., Coleman, H.G., et al. (2017). QuPath: Open source software for digital pathology image analysis. Sci. Rep. *7*, 16878. https://doi.org/10.1038/s41598-017-17204-5.

100. Pachitariu, M., Stringer, C., Dipoppa, M., Schröder, S., Rossi, L.F., Dalgleish, H., Carandini, M., and Harris, K.D. (2016). Suite2p: beyond 10,000 Neurons with Standard Two-Photon Microscopy (Neuroscience). https://doi.org/10.1101/061507.

101. Stringer, C., Wang, T., Michaelos, M., and Pachitariu, M. (2021). Cellpose: a generalist algorithm for cellular segmentation. Nat. Methods *18*, 100–106. https://doi.org/10.1038/s41592-020-01018-x.

102. Schindelin, J., Arganda-Carreras, I., Frise, E., Kaynig, V., Longair, M., Pietzsch, T., Preibisch, S., Rueden, C., Saalfeld, S., Schmid, B., et al. (2012). Fiji: an open-source platform for biological-image analysis. Nat. Methods *9*, 676–682. https://doi.org/10.1038/nmeth.2019.

Please cite this article in press as: Simon et al., Opioid-driven disruption of the septum reveals a role for neurotensin-expressing neurons in withdrawal, Neuron (2025), https://doi.org/10.1016/j.neuron.2025.04.024

STAR★METHODS

KEY RESOURCES TABLE

REAGENT or RESOURCE	SOURCE	IDENTIFIER
Antibodies		
Anti-GFP chicken antibody	Aves Lab	RRID:AB_10000240
Donkey anti-chicken 488	Jackson Immunoresearch	RRID:AB_2340375
Bacterial and virus strains		
AAVDJ-EF1a-DIO-GCaMP6s	UNC Vector core	Lot#av7830
AAVDJ-EF1a-DIO-TetTox:GFP	Palmiter Lab	N/A
AAV5-EF1a-DIO-eYFP	UNC Vector core	Lot#av4802B and Lot#AV4310L
AAV5-EF1a-DIO-eYFP	Addgene	Lot#v147551
AAV5-EF1a-DIO-hChR2-eYFP	UNC Vector core	Lot#av4313z
AAV8-EF1a-DIO-eYFP-NRN	Wu Tsai viral vector core	GVVC-AAV-164
Chemicals, peptides, and recombinant proteins		
Actinomycin-D	Sigma	Cat#A1410
Anisomycin	Sigma	Cat#A9789
OptiPrep density gradient medium	Sigma	Cat#D1556
NxGen RNAse inhibitor	Biosearch	Cat#30281-1
Morphine	UW Drug services	N/A
Naloxone hydrochloride	Sigma	Cat#N7758
Critical commercial assays		
Chromium Single Cell 3′ GEM kit v3	10x Genomics	Cat#1000075
Chromium NextGem Single Cell 3’ kit	10x Genomics	Cat#1000269
Chromium Chip B Single Cell kit	10x Genomics	Cat#1000073
Chromium NextGem Chip G	10x Genomics	Cat#1000127
Dual Index Kit TT Set A	10x Genomics	Cat#1000215
HCR probe hybridization buffer	Molecular Instruments	N/A
HCR probe wash buffer	Molecular Instruments	N/A
HCR amplification buffer	Molecular Instruments	N/A
Amplifiers 488, 546, 594, 647	Molecular Instruments	N/A
HCR probes	Molecular Instruments	N/A
TrueVIEW autofluorescence quenching kit	Vector Laboratories	Cat#SP-8400
Deposited data		
snRNAseq data: raw	This paper	GEO: GSE236007
snRNAseq data: processed	This paper	Zenodo: https://doi.org/10.5281/zenodo.15006781
HCR data: processed	This paper	Zenodo: https://doi.org/10.5281/zenodo.15006781
Experimental models: Organisms/strains		
Mouse: C57BL/6J	The Jackson Laboratory	RRID:IMSR_JAX:000664
Mouse: B6;129-*Nts*$^{tm1(cre)Mgmj}$/J	The Jackson Laboratory	RRID:IMSR_JAX:017525
Mouse: *Sst*$^{tm2.1(cre)Zjh}$/J	The Jackson Laboratory	RRID:IMSR_JAX:013044
Software and algorithms		
Prism 9	GraphPad	https://www.graphpad.com/
Cell Ranger v3	10x Genomics	https://www.10xgenomics.com/support/software/cell-ranger
Seurat v3	Stuart et al.[93]	https://satijalab.org/seurat/
Clustree	Zappia and Oshlack[95]	https://github.com/lazappi/clustree
Augur	Skinnider et al.[45]	https://github.com/neurorestore/Augur

(*Continued on next page*)

Please cite this article in press as: Simon et al., Opioid-driven disruption of the septum reveals a role for neurotensin-expressing neurons in withdrawal, Neuron (2025), https://doi.org/10.1016/j.neuron.2025.04.024

Continued

REAGENT or RESOURCE	SOURCE	IDENTIFIER
EnrichR	Kuleshov et al.[96]	https://maayanlab.cloud/Enrichr/
ImageJ	Schindelin et al.[102]	https://imagej.net/ij/
Allen Brain Cell Atlas	Yao et al.[38]	https://portal.brain-map.org/atlases-and-data/bkp/abc-atlas
HiPlex Image Registration	ACD Biosystem	https://acdbio.com/rnascope%E2%84%A2-hiplex-image-registration-software-v21
Halo	Indica Labs	https://indicalab.com/halo/qu
QuPath	Bankhead et al.[99]	https://qupath.github.io/
Suite2p	Pachitariu et al.[100]	https://www.suite2p.org/
EthoVision	Noldus	https://noldus.com/ethovision-xt
BORIS	Friard and Gamba[92]	https://www.boris.unito.it/
Original analysis code	This paper	Github: https://doi.org/10.5281/zenodo.15226356

EXPERIMENTAL MODELS AND STUDY PARTICIPANT DETAILS

Mice

Mice were housed in a 12-hour reverse light-dark cycle and provided *ad-lib* access to food and water unless otherwise noted. Both male and female mice were used in all experiments. P56-P63 mice were used in RNA-sequencing and *in situ* experiments, whereas P60 – P180 were used for *in vivo* imaging, *ex vivo* electrophysiology, and behavioral phenotyping. For all experiments, either wildtype C57BL/6J mice (Jackson Laboratories), *Nts*-Cre mice (Gifted from Zweifel & Palmiter labs, Jackson Laboratory strain #017525), and *Sst*-Cre mice (Jackson Laboratory strain # 013044) were used. All experiments were conducted in accordance with the National Institutes of Health Guide for the Care and Use of Laboratory Animals and were approved by the Institutional Animal Care and Use Committee and the University of Washington.

METHOD DETAILS

Morphine injections and precipitated withdrawal

To model opioid dependence, we used pharmaceutical-grade morphine procured from UW drug services. Mice were given an escalating dose of morphine over the course of 7 days, with each day successively increased by 10 mg/kg (10 mg/kg on day 1 through 70 mg/kg on day 7). Each mouse received two injections i.p. at each dose ~10-14 hours apart, for a total of 14 injections. Animals assigned to precipitated withdrawal received a 1 mg/kg dose of naloxone in saline (Sigma-Aldrich, #N7758) i.p. ~1 hour following their final morphine injection. Control animals only received saline. To test for acute exposure effects, we used pharmaceutical-grade morphine procured from UW drug services. Mice were given a single i.p. injection of morphine (10 mg/kg), naloxone (1 mg/kg), or saline ~1 hour prior to brain extraction.

Surgeries

Mice were anesthetized using 5% isoflurane and maintained at 0.8-1.5% isoflurane throughout each surgery. Once induced, they were head mounted in a stereotaxic frame (Kopf Instruments), and ophthalmic ointment was applied to their eyes to protect against dehydration. The incision site was injected s.c. with 1 mg/kg lidocaine, and each mouse received 5 mg/kg s.c. of carprofen, a non-opioid analgesic. We used a Nanoject (Drummond) and pulled glass pipettes (Drummond, #3-000-203-G/X; pipettes pulled using Sutter, P-87) to inject virus at a rate of 1-2 nl/sec into the LS. Coordinates and volumes used for each experiment are detailed in the following sections.

Single-nucleus RNA-sequencing and library prep

A total of 30 wildtype mice (~8 weeks) were used for single-nucleus RNA-sequencing. Animals were assigned to one of the following groups: saline (saline only), chronic morphine (escalating morphine), naloxone (escalating morphine plus naloxone), acute morphine (saline 13x, one dose of 10 mg/kg morphine) and naloxone only (saline 13x, one dose of 1 mg/kg naloxone). Each experimental group included 3 male and 3 female mice that were pooled into the same reaction.

Each day for 3 days prior to tissue collection, all animals were habituated to the procedure room for ~2 hours to control for environmentally-induced immediate early gene activity. Our procedure for tissue collection has been detailed previously.[30,31] On the day of sacrifice, mice were sequentially euthanized with sodium pentobarbital (> 90 mg/kg Somnasol) and transcardially perfused with ice-cold NMDG (96 mM NMDG, 2.5 mM KCl, 1.35 mM NaH_2PO_4, 30 mM $NaHCO_3$, 20 mM HEPES, 25 mM glucose, 2 mM thiourea, 5 mM Na+ ascorbate, 3 mM Na+pyruvate, 0.6 mM glutathione-ethyl-ester, 2 mM N-acetyl-cysteine, 0.5 mM $CaCl_2$, 10 mM $MgSO_4$; pH 7.35–7.40, 300-305 mOsm, continuously oxygenated with 95% O2 and 5% CO_2). This NMDG solution was also used for tissue

Please cite this article in press as: Simon et al., Opioid-driven disruption of the septum reveals a role for neurotensin-expressing neurons in withdrawal, Neuron (2025), https://doi.org/10.1016/j.neuron.2025.04.024

sectioning and for a collection bath. Both the perfusion solution and recovery bath included an inhibitor cocktail containing 500 nM TTX, 10 μM APV, 10 μM DNQX, 5 μM actinomycin, and 37.7 μM anysomycin, as described previously.[30] 250 μm thick coronal sections containing septum were rapidly harvested using a Leica Vibratome (VT1200). The septal complex was then rapidly microdissected, flash-frozen on powdered dry ice, and stored at -80 °C. We intended to reduce nucleus accumbens contamination as much as possible. To this end, our tissue sections primarily ranged from +1.10 mm through 0.0 mm with respect to Bregma. We also excluded the medial septum and diagonal band level to and ventral to the accumbens. Once tissue from all animals were collected and stored, we proceeded with nuclear isolation, a protocol we adapted from previously-published papers.[89,90] The following steps were all performed on ice. Also note that the PBS used here was Ca^{2+} and Mg^{2+} free. For each experimental group, we pooled all mice into the same tube containing a hypertonic lysis buffer (10mM Tris-HCl, 10 mM NaCl, 3 mM $MgCl_2$, 0.1% Igepal, 0.2 U/μl Lucigen NxGen Rnase inhibitor). Nuclei were extracted using a glass dounce homogenizer (DWK, #885300-0002) via 5-10 reps of pestle A and 5 reps of pestle B. Nuclei were then incubated in lysis buffer for 5 min. Next, the nuclear extract was moved into a clean tube, diluted to ~5-6 ml using a wash buffer (1X PBS, 1% BSA, 0.2 U/μl Rnase inhibitor), and strained into a new 50 ml conical tube using a 40 μm cell strainer (pluriSelect, # 43-50040-51). Strained nuclei were centrifuged for 10 min, 500 x g at 4 °C. The resulting pellet was then retained. To purify our nuclei, we used density gradient centrifugation, where we prepared a two-layer column containing a 25% and 30% iodixanol (OptiPrep, Sigma-Aldrich, #D1556) gradient. Briefly, we suspended the nuclear pellet in a homogenate solution (0.25M Sucrose, 25 mM KCl, 5 mM $MgCl_2$, 20 mM Tris-HCl, pH 7.8-8.0, and 0.2 U/μl Rnase inhibitor), and combined the resuspended pellet 1:1 with a 50% iodixanol solution (50% OptiPrep, 25 mM KCl, 5 mM $MgCl_2$, 20 mM Tris-HCl, 1% BSA, 0.2 U/μl Rnase inhibitor, pH 7.8-8.0) in a clean 15-ml conical tube. This creates a 25% iodixanol layer. Next, we prepare a 30% iodixanol layer (30% OptiPrep, 25 mM KCl, 5 mM $MgCl_2$, 20 mM Tris-HCl, 1% BSA, 0.2 U/μl Rnase inhibitor) and underlaid the 25% iodixanol layer with this 30% layer using a 18G needle. This density gradient column was then centrifuged for 15 min, 3000 x g at 4 °C. The resulting purified and invisible pellet was then resuspended in wash buffer. Nuclei were stained with propidium iodide and assessed for yield and quality using a disposable Neubauer hemocytometer (INCYTO, #DHC-N01) on a fluorescent microscope (Zeiss ApoTome.2). Final nuclear concentration was adjusted to 1,000 nuclei per μl in preparation for single nucleus capture.

Note that the discrepancy in kit version and sequencing platform may have obstructed our ability to compare the newer samples the older samples (saline, chronic morphine, withdrawal). Single nuclei were captured, and experimental libraries were prepared using 10X Genomics Chronium Single Cell 3′ V3 Kit (older samples) or 10X Genomics Chromium 3' NextGEM kit (newer samples). We followed the manufacturer's protocol and recommendations. Briefly, we captured ~10,000 barcoded nuclei for each experimental group and reverse-transcribed captured mRNAs to cDNA. cDNA libraries were PCR amplified, fragmented and ligated with sequencing adaptors. cDNA libraries from the older samples were sequenced on the Illumina 4400 HiSeq platform, whereas the newer samples were sequenced on the NovaSeq PE150 platform. Each sample was sequenced to a target output of ~350,000,000 reads. When introduced the two new samples (One Mor and Nal Only) into the original dataset (Sal, Mor, and Nal), cells were stably integrated into our existing clusters, which is why we retained these cells for our anatomical analyses. However, when we attempted to identify differentially expressed genes between our Sal group and One Mor or Nal only groups, we found that One Mor (acute morphine for 1 hour) induced 1,975 genes and Nal only (acute Nal only for 1 hour) induced 1,822. We found this to be unlikely to be true, because 1 week of morphine escalation (Mor) induced only 1,002 genes (Figures S2E and S2F). We believe these discrepancies may be because of differences in 10x Genomics kit versions (V3 vs NextGEM) and sequencing platform. Although there may be methods to extract some information from the newer samples, we decided that focusing on the Sal, Mor, and Nal groups for the remainder of the paper.

HCR procedure

4 male and 4 female mice were anesthetized with isoflurane and rapidly decapitated. Brains were flash-frozen within powdered dry ice and stored at -80 °C. We collected 20 μm coronal sections directly onto glass slides using a Leica CM3050S, and each slide possessed LS-containing sections from ~+1.10 through ~+0.0 Bregma. 1 slide per animal underwent HCR. We used both standard and custom-designed probes provided by Molecular Instruments, and we followed their protocol with some modifications described in our previously-published work.[30] Probes used for this experiment included *Nts*, *Sst*, *Crhr2*, *Drd2*, *Drd3*, *Foxp2*, *Esr1*, *Met*, *Tacr1*, *Pax6*, *Onecut2*, *Samd3*, *Slc32a1*, and *Slc17a6*; we also used *Fos* in activation experiments. In brief, we fixed tissue sections with 4% PFA for 30 min, and performed successive dehydration steps using 50%, 75% and 100% x 2 EtOH. Protease IV (ACDBiosystem) was used to digest tissue for 5 min, and probes were hybridized to tissue at 37 °C. We quenched autofluorescence (Vector labs #SP-8400) and mounted using VectaShield Vibrance antifade mounting media. We acquired images on a Zeiss ApoTome.2 at 10x magnification using Zen (Blue edition). Following each round, tissue was treated with DNase I (Sigma-Aldrich, #4716728001) to deplete the previous round's probes. To register all images for each section onto the same plane, we took brightfield images, which acted as the reference for each round. To validate the enrichment of *Fos* in LS-*Nts* and LS-*Met* cells following naloxone-induced withdrawal, we performed HCR on tissue from 4 mice treated with saline, 4 mice treated with chronic morphine, and 4 treated with chronic morphine plus naloxone. Each group contained 2 males and 2 females, and every slide contained 1 male and 1 female from the same group (2 slides per group, 4 mice per group). We were interested in the expression of both *Met* and *Nts*, which each ranged throughout the bulk of the septal complex, but we were limited in the number of sections we could test. Therefore, we collected serial sections from ~+0.85 through ~+0.0 Bregma, and 2 sections per mouse were retained for analysis. We imaged these sections at 20x magnification to resolve puncta. To assess the enrichment of *Fos* in LS-Nts subpopulations following acute exposure to morphine, naloxone, or saline,

we performed HCR on tissue from 6 mice treated with saline, 6 mice treated with acute morphine, and 5 mice treated with acute naloxone (1 mouse was excluded from the study due to a hematoma in the brain sample). Each group contained equal numbers of males and females, with the exception of the naloxone group which contained 2 males and 3 females. All sections were imaged with a Zeiss Apotome fluorescent microscope using a 20x objective.

In vivo two-photon imaging

4 male and 2 female *Nts*-Cre mice were unilaterally injected in the LS in two positions (rostral: +0.8 AP, - 0.35 ML, -3.0 DV; caudal: +0.2 AP, -0.35 ML, -3.0 DV) with 500 nl of AAVDJ-EF1a-DIO-GCaMP6s (UNC Vector Core, lot #av7830, titer = 2.80 x 10^{12} viral particles per ml). Following injections, a 0.6 mm x 7.3 mm GRIN lens (Inscopix) was slowly lowered and implanted into the intermediate aspect of the LS (+0.5 AP, -0.35 ML, -3.0 DV). We also implanted a metallic ring around the skull for head fixation during imaging. Once animals recovered for 3-4 weeks, we placed them on water restriction to promote motivation for sucrose consumption. For ~5-7 days, we habituated animals to head-fixation underneath the two-photon microscope, where they intermittently received 10% sucrose boli under the absence of any imaging.

Opioid dependence

For Days 0, 2, 4, 6 and 14 (1 week of opioid withdrawal) of the experiment, mice underwent structured imaging sessions. Imaging sessions were designed to first contain a 5 min baseline recording, where the animal remains idle under the 2p, followed by a 30 min session to examine LS-*Nts* evoked activity. For 30 min, mice experienced 150 trials of randomly-delivered 10% sucrose droplets (80% of trials) or 20 psi air puffs directed at the left whisker pad (20% of trials). The ITI varied from 10-15s. Following the first session (Day 0), mice were assigned to either a saline or morphine group (n = 3 for each) and received either saline or morphine injections for 7 days (Days 2, 4, and 6), and were re-imaged again on Day 14 (no opioids). Note that on these days, mice were imaged before they received morphine for the day. On Day 14, we experienced technical difficulties for 2 mice, resulting in their evoked response data dropping out for that particular timepoint.

Morphine & naloxone-induced changes of activity

Because we were also interested in the acute effects of morphine and naloxone on LS-*Nts* neurons, we designed the imaging session on Day 7 differently than the other days. Mice were first injected with either saline or 70 mg/kg of morphine. ~30 min following either saline or morphine, each mouse underwent a 5 min baseline recording and a 20 min session, where they received 100 presentations of 10% sucrose and 20 psi air puffs. Upon completion, all mice were injected with 1 mg/kg of naloxone and immediately imaged for an additional 5 min baseline and 20 min task.

All imaging was acquired using an Olympus multiphoton microscope equipped with resonant scanners and GaAsP PMTs as described previously.[31,91] We used a Mai-Tai Deep See laser system (Spectra Physics) at 920 nm wavelength for 2-p excitation. Data were collected at 7 Hz with Olympus FluoView software. Prior to each imaging session, FOVs were manually aligned with averaged projections from the previous day. Once experiments were completed, animals were euthanized using sodium pentobarbital (> 90 mg kg^{-1} Somnasol) and transcardially perfused with (1) 1x PBS and (2) 4% PFA in PBS. Brains were post-fixed for up to ~2 weeks in 4% PFA to ensure lens stability in the brain. Brains were next moved to 30% sucrose in 1x PBS for 2 days, and cryo-sectioned at 40 μm on a Leica CM3050S. To enhance and stabilize Gcamp6s signal, sections were blocked, permeabilized and then stained with 1:500 chicken anti-GFP antibody (Aves Labs, #GFP-1020) overnight at 4 °C and then with 1:1000 donkey anti-chicken 488 (Jackson ImmunoResearch, #703-545-155) for 2 hours at RT. Sections were then imaged on a confocal microscope (Olympus FV 3300).

Ex vivo electrophysiology

For patch clamp experiments, mice were bilaterally injected with AAV5-EF1a-DIO-eYFP (Addgene, Lot # v147551, titer = 1.6 x 10^{13} viral particles) and allowed to recover for 2-3 weeks. All electrophysiology experiments were performed on brain slices collected at approximately the same time of day. Mice were euthanized with an i.p. injection of sodium pentobarbital (> 90 mg/kg Somnasol). Mice were decapitated and the brain was extracted. After extraction, the brain was immersed in ice-cold NMDG ACSF (92 mM NMDG, 2.5 mM KCl, 1.25 mM NaH_2PO, 30 mM $NaHCO_3$, 20 mM HEPES, 25 mM glucose, 2 mM thiourea, 5 mM Na-ascorbate, 3 mM Na-pyruvate, 0.5 mM $CaCl_2{\cdot}4H_2O$, 10 mM $MgSO_4{\cdot}7H_2O$, and 12 mM N-Acetyl-L-cysteine; pH adjusted to 7.3-7.4) for 2 min. Afterwards coronal slices (300 μm) were sectioned using a vibratome (VT1200s, Leica, Germany) and then incubated in NMDG ACSF at 34 °C for approximately 14 min. Slices were then transferred into a holding solution of HEPES ACSF (92 mM NaCl, 2.5 mM KCl, 1.25 mM NaH_2PO_4, 30 mM $NaHCO_3$, 20 mM HEPES, 25 mM glucose, 2 mM thiourea, 5 mM Na-ascorbate, 3 mM Na-pyruvate, 2 mM $CaCl_2{\cdot}4H_2O$, 2 mM $MgSO_4{\cdot}7H_2O$ and 12 mM N-Acetyl-l-cysteine, bubbled at room temperature with 95% O2/ 5% CO2) for at least 45 mins until recordings were performed.

Whole-cell recordings were performed using a Multiclamp 700B (Molecular Devices, Sunnyvale, CA) using pipettes with a resistance of 4-6 MOhm. Pipettes were filled with an internal solution containing 100 mM cesium gluconate, 0.6 mM EGTA, 10 mM HEPES, 5 mM NaCl, 20 mM TEA, 4 mM Mg- ATP, and 0.3 mM Na-GTP with the pH adjusted to 7.2 with CsOH and the osmolarity adjusted to around 289 mmol/kg with sucrose. During recordings, slices were perfused with a recording ACSF solution (120 mM NaCl, 3.5 mM KCl, 1.25 mM NaH_2PO_4, 26 mM $NaHCO_3$, 1.3 mM $MgCl_2$, 2.4 mM $CaCl_2$ and 11 mM D-(+)-glucose, and was continuously bubbled with 95% O2/5% CO_2). Infrared differential interference contrast–enhanced visual guidance was used to select neurons that were

Please cite this article in press as: Simon et al., Opioid-driven disruption of the septum reveals a role for neurotensin-expressing neurons in withdrawal, Neuron (2025), https://doi.org/10.1016/j.neuron.2025.04.024

3–4 cell layers below the surface of the slices. LS-*Nts* or LS-*Sst* neurons were visually identified by the presence of YFP using a fluorescence microscope (Scientifica SliceScope Pro 1000; LED: SPECTRA X light engine (Lumencor)). The recording solution was delivered to slices via superfusion driven by peristaltic pump (flow rate of 4-5 ml/min) and was held at room temperature. The neurons were voltage clamped at −70 mV or +10 mV, and the pipette series resistance was monitored throughout the experiments by hyperpolarizing steps of -10 mV with each sweep. If the series resistance changed by >20 % during the recording, the data were discarded. Whole-cell currents were filtered at 1 kHz and digitized and stored at 10 KHz (Clampex 10; MDS Analytical Technologies). All experiments were completed within 4 hours after slices were made to maximize cell viability and consistency.

mEPSCs and mIPSCs were recorded in the presence of TTX (1 μM), d-AP5 (50 μM) in the recording ACSF solution. For one example recording, gabazine (1 μM) was added while holding at +10 mV to confirm observed currents were mediated by GABAA receptors. Data was analyzed with Easy Electrophysiology. For mEPSCs, a detection threshold of >10 pA and rise time <3 ms was used; for mIPSCs, a detection threshold of >10 pA and rise time <10 ms was used. Results were visually verified.

To compare the mEPSC and mIPSC frequency and amplitudes across conditions, linear, mixed-effects regressions (LMERs) were performed using the ''lmer'' function in R. Interevent interval (IEI) data was log-transformed while amplitude data was inverse-transformed to best fit a normal distribution. For statistical analysis of both IEI data and amplitude data, the linear, mixed effects regression model included group (Morphine vs Saline) as a fixed effect and mouse and cell as nested random effects. Statistical tests were performed only within data of the same cell type (*Nts* or *Sst*) and recording type (mEPSC or mIPSC). Because LMERs do not require an equal number of observations from each cell, all events from a given recording were used, with recordings typically containing 100-1000 events. Effect sizes were calculated as Cohen's d using the ''lme.dscore'' function in the ''EMATools'' package in R.

TetTox & Optogenetics behavioral profiling

For TetTox experiments, 14 *Nts*-Cre mice (6 males, 8 females) and 12 Nts-Cre mice (6 males, 6 females) were bilaterally injected with 400-500 nl of AAVDJ-EF1a-DIO-TetTox:GFP (Gifted from Palmiter lab, titer = 4.2 x 10^{12} viral particles per ml) or AAV5-EF1a-DIO-eYFP (UNC Vector Core, lot #av4802B, titer = 4.40 x 10^{12} viral particles per ml) in the LS (0.6 AP, ± 0.40 ML, -2.80 DV), respectively. The virus was allowed to incubate for at least 8 weeks before any behavioral testing. Following this recovery period, baseline testing occurred over 1-2 weeks. For optogenetics, 12 male *Nts*-Cre mice were bilaterally injected with 400 nl of AAV5-Ef1a-DIO-hChR2-eYFP (UNC Vector Core, lot #AV4313z, titer = 3.2 x 10^{12}) or AAV5-Ef1a-DIO-eYFP (UNC Vector Core, AV4310L) into the LS (0.38 AP, ± 0.45 ML, -2.90 DV), and received bilateral implantation of optical fibers (RWD Life Science, Inc; 907-03007-00) over the same site (10°, 0.38 AP, ± 1.01 ML, -2.86 DV). Mice were allowed to recover for ∼4 weeks prior to baseline testing. All mice underwent morphine escalation as described in other experiments. On completion of the drug course, behavioral testing resumed for up to 4-5 weeks. Prior to each day's testing, all mice were acclimated to the room for 30 min – 1 hour. Recordings were captured under an infrared light source and tracked via Noldus Ethovision XT11, unless otherwise noted. For optogenetic experiments, in general, blue laser light was delivered at 20 Hz frequency and with 5 ms pulse durations.

Open field

Mice were allowed to explore a standard open field for 10 minutes and were recorded from overhead. The first 5 minutes of data were retained for analysis. For optogenetic experiments, laser light was for 5 min durations followed by 5 min light off epochs (two cycles).

Elevated plus maze (EPM)

Mice were allowed to explore a standard EPM setup (34.3 cm height, 63.5 cm length of each arm, 17.8 cm high wall on closed arms) for 10 min. Annotated zones included open and closed arms, as well as the center of the EPM. The first 5 minutes of data were retained for analysis. For optogenetic experiments, laser light was delivered throughout the entire duration of the EPM test.

Sucrose preference

We used Med Associates chambers and voltage lickometers to assess each animal's preference for tap water or 2% sucrose solution. Mice were habituated to Med Associates chambers for 2-3 sessions, 30 min – 1 hr each, prior to the test session, and test sessions were 1 hr long.

Social preference

To test for differences in social proclivities, we used a 3-chamber setup in which subjects were presented with an unfamiliar mouse on one side and an unfamiliar object on the other. Mice were first habituated to the 3-chamber apparatus with nothing in either side, and on the following day, they were exposed to a same-sex, weight-matched mouse and a 3D printed mouse for 10 min.

Hot plate

Mice were exposed to a hot plate (BioSeb) for 30 s at 55 °C to evaluate pain-coping behaviors, including hind-paw licks and jumps. Recordings of all animals were coded and blindly scored, and BORIS[92] was used for behavioral annotation and quantification.

Please cite this article in press as: Simon et al., Opioid-driven disruption of the septum reveals a role for neurotensin-expressing neurons in withdrawal, Neuron (2025), https://doi.org/10.1016/j.neuron.2025.04.024

Withdrawal signs

To assess differences in withdrawal signs, mice were injected with 1 mg kg^{-1} of naloxone 1 hour following their final dose of morphine. They were immediately placed into an empty cage and recorded from the side for 20 min. Recordings of all animals were coded and blindly scored for withdrawal signs, and BORIS[92] was used for behavioral annotation and quantification. Withdrawal signs included fecal boli, jumping, and bouts of lethargy.

Resident intruder assay

We performed a resident intruder assay ~2 months of opioid withdrawal. A young (~12 week) same-sex albino mouse (C57BL/6J) was placed into the home cage of each resident mouse for 6 min, and social interactions were recorded from the side. Videos were scored using BORIS, and we measured the following behaviors of the resident mouse: nose-to-nose sniffing, anogenital sniffing, fleeing, digging, and huddling. Notably, there were no attack bouts. For optogenetic experiments, laser light was introduced in 2 min light on/light off epochs.

SHIELD Tissue clearing

To label LS-*Nts* projections, 4 *Nts*-Cre mice were unilaterally injected with 200 nl of AAV8-EF1a-DIO-eYFP-NRN (Stanford Virus Core, cat# GVVC-AAV-164, 3.08 x 10^{13} viral particles per ml, 1:1 dilution with saline) in the LS (+0.60 AP, 0.40 ML, -2.80 DV). Three weeks following viral injection, mice were perfused with 1x PBS and 4% PFA-PBS, after which the brain was harvested and post-fixed with PFA for 24 hours. After post-fixation, the brains were processed following the SHIELD tissue clearing protocol (LifeCanvas). Briefly, the brain was incubated in SHIELD OFF solution [2.5 mL DI water, 2.5 mL SHIELD-Buffer Solution, 5 mL SHIELD-Epoxy Solution] at 4°C for 4 days. Then transferred to SHIELD ON buffer and incubated at 37°C for 24 hrs. Following, SHIELD ON buffer incubation, the brain was pre-incubated in Delipidization buffer for overnight at room temperature. The tissue was then placed into SmartClear (LifeCanvas) to conduct active tissue clearing for 24 hours. To match the refraction index, the tissue was incubated in 50% of EASI-INDEX solution (RI = 1.52, LifeCanvas) at 37°C for 24 hrs and then 100% of EASI-INDEX solution at 37°C for 24 hrs. The tissue was then embedded in EASI-INDEX agar and mounted onto SmartSpin light sheet microscope (LifeCanvas). Tissue was imaged from the horizontal view using a 3.6x objective with 4 μm zstep. Images were registered to a standard brain atlas (Chon et al., 2019) using ClearMap pipeline (Renier et al., 2016) on a cluster computer. eYFP expressing puncta spots were segmented through the same pipeline using a classifier created using Ilastik (Berg et al., 2019). The total number of eYFP positive puncta spots per brain region in the injection ipsilateral hemisphere was quantified.

QUANTIFICATION AND STATISTICAL ANALYSIS

General statistics

Statistical methods and results were reported in each figure. Data generated from our TetTox experiments were analyzed using Prism v9.4.1. Generally, we performed repeated measures two-way ANOVA followed by Sidak's multiple comparisons correction. Some analyses leveraged linear regression to compare y-intercepts and slopes among different groups and timepoints, where noted. Sequencing and calcium imaging data were analyzed using both published pipelines and custom Python and R scripts.

Single-cell RNA-sequencing clustering and gene expression analysis

Once sequenced, reads were aligned to a pre-mRNA reference genome using the 10X Genomics' Cell Ranger v3 pipeline, which provided digital expression matrices that were used for downstream analysis. Clustering, sample integration, cell type identification, and differential gene expression identification were all carried out using the Seurat V3 R package.[93]

Filtering and quality control

We have previously published our general filtering parameters,[30,31] but in brief, genes expressed in fewer than 3 cells were removed from the dataset. We next retained cells that possessed between 500 and 25,000 UMIs and fewer than 1% mitochondrial read enrichment. Although we included the cutoffs normally used for scRNA-seq, snRNAseq data are mostly depleted of mitochondrial reads. Doublets were then computationally predicted and removed by the DoubletDecon R package[23] using the default parameters.

Sample integration and clustering

Once putative doublets were omitted, we utilized Seurat's integration algorithm based on canonical correlation analysis[24] and mutual nearest neighbor analysis.[25] Gene transcript counts were scaled for total sequencing depth (factor of 10,000) and then natural-log transformed. Integration anchors were identified for each dataset and transformed by a correction vector to produce a "corrected" expression matrix, on which we performed principal component analysis (PCA). We used the first 30 PCs to identify cell clusters (using Louvain, resolution 0.80) and to plot their proximity in space using Uniform Manifold Approximation and Projection (UMAP). We evaluated the expression of canonical neuronal markers (e.g. *Stmn2* and *Thy1*) to identify neuronal populations, and proceeded to subset these neurons out of the data and performed re-clustering to reveal intra-neuronal heterogeneity. In re-clustering neurons, we normalized and scaled expression data using scTransform,[94] which constructs a generalized linear model (GLM) to dissociate sequencing depth from gene expression without reducing cell type heterogeneity. We integrated datasets and clustered individual

Please cite this article in press as: Simon et al., Opioid-driven disruption of the septum reveals a role for neurotensin-expressing neurons in withdrawal, Neuron (2025), https://doi.org/10.1016/j.neuron.2025.04.024

neurons based on these transformed data as described before, but used the original, linearly-scaled and normalized RNA values in downstream expression analyses.

To determine the optimal clustering resolution for our data (i.e. number of bioinformatically-determined neuron types), we utilized the Clustree R package.[95] This approach allowed us to assess the stability of clusters over a series of clustering granularities. We determined 14 clusters (2 glutamatergic and 12 GABAergic at a resolution of 0.20) to be optimal because it produced stable clusters with neurons yielding from each experimental group. Although it appears that perhaps a lower resolution would produce even more stable clusters (resolution = 0.10), we selected the higher value because we believe that Gaba12 neurons are bona-fide septal cells, distinct from Gaba7. They are however rare and so do not separate as readily as other cells might. Next, to identify potential molecular markers for each cell cluster, we computed the average expression of a given gene in one cluster, and then compared it to the expression of that gene in all other clusters combined. P-values were computed using Wilcoxon rank sum test and corrected for the total number of genes tested.

DEG analysis

To understand what transcriptional changes were induced by chronic morphine treatment, we first collapsed cell types into single pools separated by condition (Sal, Mor, and Nal). We did this first because presumably the most robustly altered DEGs would be enriched in pseudobulk. We performed a series of pairwise comparisons across all genes between two experimental groups (Sal vs Mor; Mor vs Nal) and retained genes with an average logFC of at least 0.1 and p-value < 0.05 (Wilcoxon rank sum test following by Bonferroni post-hoc correction). We then took this list of pseudobulk DEGs and split them as either upregulated (logFC > 0.1) or downregulated (logFC < -0.1) and fed these lists through EnrichR for GO analysis.[96–98] We referred to the top 10 GO terms to derive a list of glutamate receptors, GABA receptors, potassium channels, and calcium channels, and we subsequently calculated the average logFC between Mor and Sal, such that positive logFC values indicated enrichment in Mor (Wilcox rank sum test followed by Benjamini-Hochberg false discovery rate, adjusted for the number of cell clusters tested; n = 14).

We also wanted to understand which morphine-induced DEGs may change in a cell type-specific manner. To do this, we identified Mor-induced DEGs for each cell cluster because we wanted to capture DEGs that may be uniquely altered on a cell cluster basis. We then concatenated the DEGs identified from every cell cluster and took the fold-change difference between these two datasets, resulting in a Δ expression matrix for saline versus morphine. Dimensionality of this data frame was reduced via PCA, and the feature ranking (genes) from PC1 was retained and plotted as a heatmap. We identified enriched ontology terms using EnrichR.[96] Note that we removed Gaba12 from this analysis because it was transcriptionally distinct from the other cell types, thereby skewing the variability of DEG expression.

To determine a DEG enrichment score for Sal vs Mor, we randomly sampled at most 100 cells from each neuron cluster and summed both up- and down-regulated DEGs into one value. This is because there is an innate correlation between the number of cells per cluster and the number of DEGs that will be identified; limiting the number of tested cells for each cluster limits this bias. These values were normalized across cell types in each comparison, such that the lowest DEG total was 0 and the highest was 1. We approached the Mor vs Nal comparison differently because gene expression differences were much more subtle these two groups. To ensure our DEG metric for Mor vs Nal was stable, we randomly sampled 100 cells from each cell type and each group to compute the total number of DEGs and repeated this 100 times. We took the normalized average number of DEGs as the score for Mor vs Nal.

IEG analysis

We used a predetermined list of IEGs implicated in the literature.[27] From this list, we first subset genes that were present in our LS data and calculated the average expression difference between Mor and Nal of each gene in each cluster and subsequently tested whether the difference in expression between Mor and Nal was significant (Wilcox rank sum test followed by Benjamini-Hochberg false discovery rate, adjusted for the number of cell clusters tested; n = 14). In Figure 3, we plot only the genes that were significantly altered by precipitated withdrawal in any cell cluster. To determine a singular metric for neuronal activation post-naloxone, we first averaged the expression of the panel of significantly altered IEGs within each cell type (single IEG average for every cell), then subsequently tested whether this average was statistically different between Mor and Nal conditions (Wilcox rank sum test followed by Bonferroni post-hoc correction). We performed the same analysis with *Fos*, *Fosb*, *Egr1*, *Jun*, *Junb, Jund, Arc*, and *Nr4a1*.

Classifier analysis

We performed pairwise comparisons between Sal and Mor and then Mor and Nal to compute AUC, a measure of classifier accuracy, using the R package Augur.[45] The classifier's accuracy is related to how transcriptionally "distinguishable" Sal and Mor cells or Mor and Nal cells are from each other, but it does not explicitly test whether cells contain altered Morphine or Naloxone-related genes. In brief, Augur subsamples 20 random cells from each cell cluster and withholds their experimental group label (Sal, Mor, and Nal), essentially blinding the classifier to which condition that cell was subjected to. Next, it trains a classifier on the gene expression matrices of the remaining cells—with intact experimental group labels—in each cell cluster. Finally, we tested whether the classifier can accurately determine which experimental group each of the original 20 cells belong to, producing an AUC score. This process is repeated 50 times to produce a cross-validated AUC score that we use to determine whether Morphine and Naloxone differentially alter each cell cluster. This analysis was rooted in the assumption that the classifier will be more accurate if cells between each

condition are more transcriptionally distinct. Lower AUC scores indicate that cells between two conditions are more similar. AUC scores across 150 iterations were plotted for Sal vs Mor and Mor and Nal and statistically tested for differences against a shuffled control (Sal vs Mor, but group labels for each cell were randomized).

HCR analysis

All images acquired for HCR were registered and cropped using ACD Biosystem's HiPlex image registration software, with brightfield images used as a reference. We used Indica Labs HALO v3.2 to perform multi-channel *in situ* spot quantification. Parameters for detecting puncta and intensity of each gene were manually adjusted for each tissue section of each animal. Cells were considered positive for a particular gene if they possessed 5 or more copies. Cell type abundance and spatial distributions were calculated using custom R scripts.

Correlation between snRNAseq and HCR

To evaluate the congruency between snRNAseq and HCR datasets, we first clustered the *in situ* data. We performed supervised clustering by feeding the HCR dataset into Seurat as a digital expression matrix. This HCR-based expression matrix contained single cells detected across all 8 animals and the spot counts for every gene; we also included signal intensity measurements as metadata. Once loaded, the HCR digital expression matrix was scaled but not normalized. During scaling, we regressed out gene intensity measurements on the basis that signal intensity may indicate staining quality. Next, cells were clustered using the same pipeline as described above. We manually identified which HCR cluster corresponds to each snRNAseq cluster based on relative expression of predicted cell type markers. We computed the percent of cells expressing every candidate gene in each cluster and correlated gene enrichment between HCR and scRNAseq datasets via Pearson correlation.

Calculating naloxone-induced IEG expression changes

To measure *Fos* induction in LS-*Nts* and LS-*Met* neurons, we collapsed cells from all animals in each experimental group. The experimenter adjusting HALO detection parameters for every gene was blinded to the experimental group of each tissue section. Any cell containing the top 15th percentile of spot counts for *Nts* and *Met* were determined to be *Nts*+ or *Met*+, respectively. However, puncta for IEGs did not undergo thresholding and were instead treated as distributions. Once spot counts were determined for all sections and animals, 2-3 sections per animal were retained for analysis, and all cells from all animals were collapsed into the same dataset. Determining whether Nal induces IEG expression required us to perform a linear mixed effects model to account for variance associated with animal and sex (fos.Copies $\sim$ group + (1 | sex) + (1 | slide) + (1 | animal)). We also collapsed all cells into Sal, Mor and Nal groups and compared relative distributions of each gene within each cell type using the Kolmogorov-Smirnov test (CDF included 10 bins). We chose not to run statistical testing on the median expression of each gene (of collapsed cell data) because the n was high enough to induce significance in any comparison.

Calculating acute morphine or naloxone-induced IEG expression changes

Due to lack of open-source access to HALO, we instead used QuPath v0.3.2: Open source software for digital pathology image analysis to perform multi-channel *in situ* probe quantification.[99] Each image was coded to blind the experimenter to the treatment group. DNA stain via DAPI was used for LS ROI mapping and individual cell boundary detection where we created a 3μm extended border to include probe detection at the cell membrane. Parameters for positive detection of each probe within a cell were manually thresholded by fluorescent intensity and background for each tissue section of each mouse. Cells were binarized as positive or negative for a given gene marker. Given our results from naive and chronic exposure groups, we primarily focused our analyses on LS-*Nts Met* expressing cells. Statistical analysis included Ordinary one-way ANOVA for single gene comparisons and mixed effects model to account for variance associated with distribution across the anterior-posterior axis. We also collapsed all cells within each treatment group to compare relative distributions of *Nts* subpopulations. All datasets were normally distributed according to Bartlett's test.

Two-photon analysis

Raw calcium imaging files were exported as a series of.TIFF images and loaded into Suite2p[100] for motion correction, ROI detection and signal extraction. Motion correction was performed using nonrigid registration with a 300-frame averaged reference, and an integrated CellPose[101] plugin was used to automate ROI detection. We manually annotated cells that were not detected. Due to high correlation between raw fluorescence traces and output neuropil signals, we elected to not perform neuropil correction and instead retained only the raw fluorescence trace for downstream analysis. We were concerned that because LS-*Nts* are relatively sparse, the neuropil signal may be contaminated by the cell itself.

Spontaneous activity analysis

Assessing withdrawal-induced alterations in spontaneous activity required us to detect discrete calcium events in our data. To achieve this, we wrote a custom Python script to perform the following transformations to each calcium trace: (1) rolling mean over 20 frames, (2) baseline correction using a polynomial fit, (3) Z scoring across the trace, (4) Buttersworth lowpass filter in both forward and reverse directions to correct for time lag, and (5) peak detection via SciPy Signal package. Due to preprocessing and filtering, we did not threshold peaks by amplitude in the final step.

Please cite this article in press as: Simon et al., Opioid-driven disruption of the septum reveals a role for neurotensin-expressing neurons in withdrawal, Neuron (2025), https://doi.org/10.1016/j.neuron.2025.04.024

Evoked activity analysis

Within each calcium trace, we identified epochs when (1) sucrose or (2) air puffs were delivered and identified peri-stimulus time histograms (PSTHs) for every event, similar to how we have reported before.[91] When calculating ΔF/F, we used the 2.5 s period between the trial start and stimulus delivery as a the F_0 (baseline). For reported Z scores, we performed Z scoring across the mean PSTH for every cell. To determine whether a cell is responsive to each stimulus, we used a Wilcoxon signed rank test on its baseline activity (F_0) versus its evoked activity on every trial. Multiple comparisons for each cell were adjusted using Bonferroni post-hoc correction. We then counted the number of cells deemed responsive ($p < 0.05$) and performed Fisher's Exact Test to determine whether morphine dependence alters LS-*Nts* responsivity to sucrose and air puffs. Finally, to compute AUC, we used a linear trapezoidal method over 5 s following stimulus presentation.